

The Low Frequency Radio Counterpart of the XMM Large Scale Structure Survey

A. S. Cohen ^{1,3}, H. J. A. Röttgering ², N. E. Kassim ¹, W. D. Cotton ⁵, R. A. Perley ⁴,
R. Wilman ², P. Best ⁷, M. Pierre ⁶, M. Birkinshaw ⁸, M. Bremer ⁸, and A. Zanichelli ⁹

ABSTRACT

The XMM Large Scale Structure Survey (XMM-LSS) is a major project to map the large scale structure of the universe out to cosmological distances. An $8^\circ \times 8^\circ$ region will be surveyed by XMM with planned optical follow-up to produce a three-dimensional map of many hundreds of clusters out to a redshift of $z = 1$. To explore the relation of the large scale structure to the location and properties of extragalactic radio sources, the XMM-LSS project also includes a low frequency radio survey of this region. This combination will provide unprecedented insight into how the radio source formation and evolution are affected by the local environment. Here, we present preliminary results from our 325 MHz and 74 MHz surveys in this region. At 325 MHz, we have a flux limit of 4 mJy/beam, a resolution of $6.3''$, and a total of 256 source detections over 5.6 square degrees. At 74 MHz, we have a flux limit of 275 mJy/beam, a resolution of $30''$, and a total of 211 source detections over 110 square degrees. We describe these results and explore what they tell us about the population of extra-galactic low frequency radio sources. The 74 MHz survey represents the first presentation of a deep, sub-arcminute resolution survey at such a low frequency. This was made possible

¹Naval Research Laboratory, Code 7213, Washington, DC, 20375 USA, cohen@rsd.nrl.navy.mil, kassim@rsd.nrl.navy.mil

²Leiden University, Sterrewacht, Oort Gebouw, P.O. Box 9513, 2300 RA Leiden, The Netherlands, rottgeri@strw.LeidenUniv.nl

³National Research Council Postdoctoral Fellow

⁴National Radio Astronomy Observatory, P.O. Box 0, Socorro, NM 87801 USA

⁵National Radio Astronomy Observatory, 520 Edgemont Road, Charlottesville, VA, 22903 USA

⁶Saclay

⁷Institute for Astronomy, Royal Observatory Edinburgh, Blackford Hill, Edinburgh, EH9 3HJ, UK

⁸Department of Physics, University of Bristol, Tyndall Avenue, Bristol BS8 1TL, UK

⁹Istituto di Radioastronomia - CNR, Bologna, Italy

by recent advances in both hardware and data reduction algorithms which we describe in detail.

1. Introduction

The XMM Large Scale Structure Survey (XMM-LSS) is a deep X-ray survey designed to map the distribution of groups and clusters of galaxies out to a redshift of $z = 1$ (Pierre et al. 2001). This will provide an unprecedented view of the large scale structure of the universe. For the first time, the cluster correlation function will be measured for high redshifts. The planned optical follow-up will compare the spatial distribution of AGNs with this large scale structure, and study the origin of AGN/QSO and how it relates to its surroundings. Comparison of the cosmic web determined from X-rays with the galaxy distribution determined optically will shed light on bias mechanisms as a function of redshift.

The XMM-LSS survey consists of a 24×24 grid of XMM pointings, each with 10 ks integration, that will uniformly map a square $8^\circ \times 8^\circ$ region to a sensitivity for point-like sources of about $5 \times 10^{-15} \text{ erg cm}^{-2} \text{ s}^{-1}$ in the [0.5-2] keV band. A thorough study of the expected number of clusters detected by this survey was recently carried out by Refregier, Valtchanov, & Pierre (2002). Using the non-evolving luminosity temperature (L-T) relation of Arnaud & Evrard (1999), the Press-Schechter formalism (Press & Schechter 1974) and X-ray image simulations, the number of detectable clusters was predicted as a function of redshift for various cosmologies. In the favored Λ CDM cosmology, they predict that XMM-LSS should detect about 600-1200 clusters within $0 < z < 1$ and another approximately 300 at $1 < z < 2$.

An optical follow-up in the XMM-LSS region is planned with the MEGACAM at the CFHT. Deep ($I \approx 25$) imaging of the entire region will detect a sufficient number density of galaxies to allow for weak lensing detections of large filaments. A planned spectroscopic follow-up program will measure the redshifts for all candidate clusters identified in the X-ray survey.

With the prospect of these data, we conducted a low-frequency VLA survey of the XMM-LSS region in order to investigate the relationship between the population of cosmological radio sources and the large scale structure of the universe. Specific questions we wish to address include: (i) Where are various populations of radio sources and X-ray quasars located with respect to the LSS? (ii) How does the environment of radio sources influence their fundamental physical properties such as linear size and radio power? (iii) What is the connection between distant Mpc-sized radio halos and the dynamical state of their associated

clusters?

Our low-frequency radio survey was conducted with the VLA in the A-array configuration and mapped the entire XMM-LSS region at 74 MHz and 5.6 square degrees of this region at 325 MHz. This was made possible by recent advances in low-frequency imaging including the addition of 74 MHz receivers to the VLA in 1997, and the development of new software and data reduction algorithms which make it possible to map the entire primary beam at these frequencies.

At 325 MHz our limiting flux density ($5\sigma_{rms}$ level, where $\sigma_{rms} \equiv$ map rms) is 4.0 mJy and our resolution is $6.3''$. For comparison, the WENSS survey (Rengelink et al. 1997), conducted at 325 MHz and 352 MHz, which covers the northern sky above $\delta = +30^\circ$ has a limiting flux density of about 18 mJy/beam with a resolution of about an arcminute. A deeper survey of a smaller area (95 square degrees) at 327 MHz has been done at Westerbork (Wieringa 1993), reaching about 3 mJy/beam over 95 square degrees, though also at one arcminute resolution. The 365 MHz Texas survey (Douglas et al. 1996) covers the sky between $-35.5^\circ \leq \delta \leq +71.5^\circ$, but only reaches a depth of 250 mJy/beam.

Though no published surveys exist at 74 MHz, we can compare our sensitivity to surveys at 38 MHz and 151 MHz by assuming a typical spectral index. If we apply a spectral index of $\alpha = -0.7$ ($S \propto \nu^\alpha$), our 74 MHz limiting flux density of 275 mJy/beam becomes 170 mJy/beam at 151 MHz and 440 mJy/beam at 38 MHz. Using this standard, our 74 MHz observation is about twice as deep as the 38 MHz 8C survey (Rees 1990), about 20% more sensitive than the 151 MHz 6C survey (Hales, Baldwin, & Warner 1988) but only about 60% as sensitive as the 151 MHz 7C survey (Vessey & Green 1998). Our resolution is about an order of magnitude better than the 6C and 8C surveys and about a factor of 3 better than the 7C survey. Figure 1 shows the sensitivity and resolution of our XMM-LSS radio surveys at both 74 MHz and 325 MHz in comparison to major low frequency radio surveys.

As figure 1 shows, at both frequencies, our survey has a unique combination of both depth and resolution. The high resolution was desirable to help classify radio sources (eg. compact versus double lobe), to reduce classical confusion, and to allow better optical identification. Using customized source-finding software, we identified and characterized 211 sources at 74 MHz and 256 sources at 325 MHz, many of which are resolved doubles.

This paper will be organized as follows: Section 2 will describe our observation strategy, and Section 3 will explain in detail our data reduction procedure. Our source finding method will be covered in Section 4. That will be followed by a description of the results (Section 5), error analysis (Section 6) and survey completeness (Section 7). We end with our conclusions and future plans in Section 8.

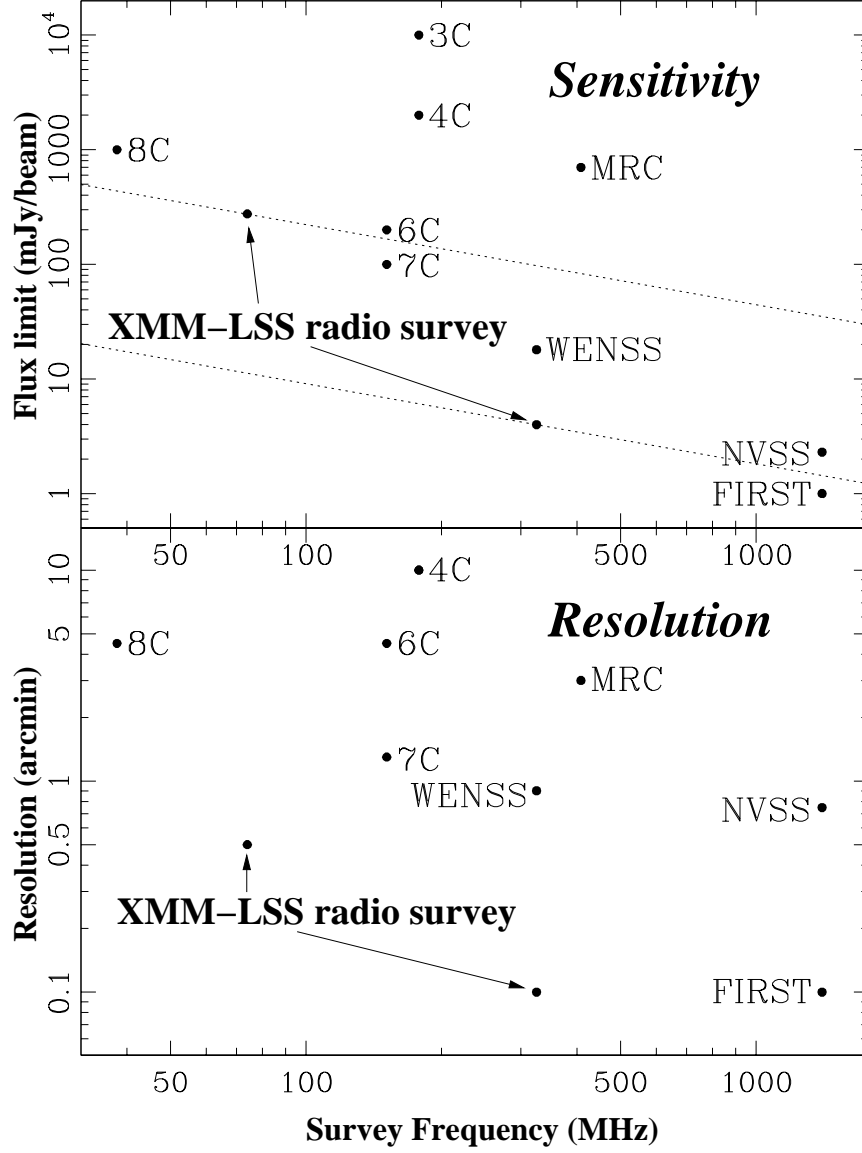


Fig. 1.— The sensitivity and resolution of our XMM-LSS low frequency radio survey compared to that of the major low frequency radio surveys. The dotted lines on the sensitivity plot (top) are lines of “constant” limiting flux assuming a spectral index of $\alpha = -0.7$.

2. Observations

2.1. Field Selection

For the XMM-LSS survey, a field location was chosen centered at $RA = 2^h16^m$ and $\delta = -5^\circ$ mainly because of its high galactic latitude ($b = -58^\circ$), low N_H and high XMM visibility (about 20%). An additional consideration was easy visibility from both the northern and southern hemispheres for follow-up from globally dispersed observatories.

At 325 MHz, the primary beam is 2.68° (FWHP) in diameter which can only cover about 6% of the XMM-LSS region. Therefore, we pointed at the location which would best cover the area guaranteed to be imaged in the first round of XMM-LSS observations. Our pointing center was at $RA = 2^h24^m40.0^s$ and $\delta = -4^\circ30'0.0''$. At 74 MHz, the primary beam has an 11.9° diameter (FWHP) and the entire XMM-LSS field is covered.

2.2. Observation Strategy

The large fields of view involved caused us to consider the non-coplanar nature of the VLA for non-snapshot observations. The geometric distortion caused by the non-coplanar nature of the VLA leads requires a 3-D, rather than 2-D, Fourier inversion of the visibility data to produce sky maps. This is a computer-intensive process, although it is tractable, with the greatest computational burden arising from observations with the target at low elevations. In order to reduce the computational burden we therefore chose to observe in two 4-hour runs centered at transit on two different days, rather than a single 8-hour run. We observed simultaneously at 325 MHz and 74 MHz with bandwidths of 6 MHz and 1.5 MHz respectively. With these configurations, bandwidth smearing would prevent us from imaging the entire primary beam of the VLA at either frequency in continuum mode. In fact the field of view in which bandwidth smearing expands the width of sources by less than a factor of two is only 0.37° and 1.4° for 325 MHz and 74 MHz respectively, a small fraction of the primary beam diameter for each, 2.68° and 11.9° respectively. Therefore, we observed in spectroscopic mode to avoid problems of bandwidth smearing and to allow more efficient removal of radio-frequency interference (RFI). At 74 MHz, the central frequency was 73.8 MHz, and we used 128 channels, each of width 12.2 kHz. At 325 MHz, we used 32 channels each of width 193.3 kHz. We centered the 325 MHz observations for each 4-hour run at slightly different frequencies, 321.5 MHz and 328.5 MHz, in order to improve the combined uv coverage. We observed with an integration time of $\Delta t = 6.6$ seconds, the shortest possible with our frequency configuration. This caused the predicted reduction in peak flux from time-smearing at the primary beam half power point to drop from 4% (with

the standard $\Delta t = 10s$) to 1.8% (with $\Delta t = 6.6s$). Our total time on source was 5.3 hours. Observations took place on January 5th (LST 0100 to 0500) and January 12th (LST 0030 to 0430) of 2001.

3. Data Reduction

3.1. Initial Calibration and RFI Removal

At both 74 MHz and 325 MHz, we first performed a bandpass calibration on Cygnus A. As Cygnus A is resolved, we referenced the calibration to models taken from previous observations at each frequency, scaled to match the absolute flux density measurements of Baars et al. (1977). We then performed an amplitude and phase calibration. For the 325 MHz data, we used the flux and phase calibrators 3C48 and J0204+152, respectively, while at 74 MHz we used Cygnus A for both flux and initial phase calibration.

After calibration we focused on RFI removal. For this, we used the AIPS task FLGIT, in which one can set overall clipping levels for the spectral data as well as remove data which fall too far off a linear spectral fit. In practice, this removes most of the RFI which is strong enough to noticeably degrade the final image. We experimented with the FLGIT parameters to find an acceptable balance between removing all the clearly bad data and keeping most of the unaffected data. For the 325 MHz data, we clipped every baseline visibility ($\Delta t = 6.6s$, $\Delta \nu = 193.3kHz$) above 20 Jy. For the 74 MHz data, we clipped all visibilities ($\Delta t = 6.6s$, $\Delta \nu = 12.2kHz$) that were either above 1,200 Jy or more than 500 Jy off the spectral fit. The predicted noise levels per visibility per channel are approximately 140 Jy and 2.8 Jy for 74 and 325 MHz respectively. As these clip levels are well above the total flux in each field as well as the noise levels, we are certain to have only removed corrupted data. This removed 15.5% and 4.0% of the 74 MHz and 325 MHz data respectively.

3.2. 325 MHz Data

At 325 MHz, we removed three channels from each end of the bandwidth at both frequency settings, where the gains are too low to achieve reliable calibration. We were left with 25 channels, each of width 193.3 kHz. No channel averaging was done because that would have introduced noticeable bandwidth smearing toward the edges of the field, already at 4% without any averaging. For each baseline, each channel is counted as a separate visibility. Final flagging was done by hand with the AIPS task TVFLG in order to remove any remaining data which appeared corrupted, resulting in the removal of less than 1% of

the remaining data.

The data from all channels were combined to produce images. As the effects of a non-coplanar array become unmanageable in a field this large, the entire primary beam cannot be imaged at once with a standard 2D Fourier inversion. Instead a pseudo-3D treatment (Perley 1999) was implemented in which we divided the primary beam area of diameter 2.68° into 439 smaller fields (facets) each 350×350 pixels with a $1.5''$ pixel spacing. For each facet, the phase center is reset to the center of that facet, and the synthesized beam used for deconvolution is recalculated for that location. When combined, the facets cover the entire primary beam area in a single map 6000 pixels across. Since bright sources outside the primary beam can cause sidelobe confusion in this map area, we also imaged an additional 49 facets outside the primary beam which contained bright NVSS sources, so that their sidelobes could be cleaned from the region of interest. Deconvolution was performed with the CLEAN algorithm (Högbom (1974), Clark (1980)).

Before imaging, phase only self-calibration was done according to a model of the source distribution in the primary beam predicted by applying a spectral index of $\alpha_{325}^{1400} = -0.75$ to the NVSS catalog. The AIPS task FACES was used to create this model. Though assuming a constant spectral index is not completely realistic, in practice this method generally produces adequate phase calibration for an initial image. A further advantage to this method is that it removes any overall position shift in the field due to the ionosphere, which is generally of order $\sim 10''$ at 325 MHz. Later, we performed two further iterations of phase-only self-calibration with the actual 325 MHz image, for further refinement. The resulting image had an off-source RMS noise of 0.8 mJy/beam at the field center. Since the thermal noise is predicted to be 0.3 mJy/beam and classical confusion noise is negligible at this resolution, the sensitivity of the image is most likely sidelobe-confusion limited. We corrected the primary beam attenuation away from the field center by dividing by the primary beam pattern with the AIPS task PBCOR. This caused the noise level to increase toward the edges of the primary beam region. The synthesized beam size was $6.3'' \times 5.3''$, and the image was convolved to a circular $6.3''$ resolution for source finding.

3.3. 74 MHz Data

At 74 MHz, as for 325 MHz, we removed channels from the edges of the bandwidth which appeared to be of poor quality. We were left with 120 channels, of which every 5 were averaged to produce 24 channels, each of width 61.0 kHz. We did not average any further as the bandwidth smearing at the field edge for this channel width is already 7%. Final flagging, in addition to the previous use of FLGIT on the initial spectral data, was done

by hand with TVFLG in order to remove any remaining data which appeared corrupted, resulting in the removal of less than 1% of the remaining data.

Checking the field beforehand against the NVSS database showed there to be one dominant source in this field, 3C63 (source J0220.9–0156 in Tables 3 and 4). This source’s flux density was previously measured to be 34.0 Jy at 80 MHz (Wright & Otrupcek 1990). Preliminary phase-only self calibration was performed by mapping only this source. We then included other sources in the field into the model, anticipating that this would improve the self-calibration as it had for the 325 MHz data. This turned out not to be the case for 74 MHz. The assumption fails because of the breakdown at this frequency of the basic assumption of conventional self-calibration, that the ionospheric phase distortions over the field of view can be characterized by one time variable number per antenna. This is because lines of sight through the ionosphere to sources on opposite sides of the large field of view are separated by large linear distances over which the ionosphere’s properties differ. This radio-frequency “seeing” limitation is referred to as the breakdown of the “infinite isoplanatic patch assumption” and angle independent self-calibration is not applicable.

3.3.1. *The Ionosphere at 74 MHz*

The ionosphere, which has a significant but manageable effect at centimeter wavelengths, causes such large phase distortions at low frequencies ($\nu < 150$ MHz), that this region of the electromagnetic spectrum has remained unexplored at sub-arcminute resolution until the relatively recent onset of the 74 MHz VLA (Kassim, Perley, & Erickson (1991); Kassim, Perley, Erickson, & Dwarkanath (1993)). Because of this and the fact that the ionosphere is the primary issue in 74 MHz data reduction, we will explain some of the main issues involved in this section.

A low frequency interferometer is extremely sensitive to *differences* in the total electron content (TEC) above pairs of antennas. For our discussion of the effects of the ionosphere on the 74 MHz data, the ionosphere can be approximated by a thin screen phase delay model which varies in both space and time across the field of view. At the height of the ionosphere (which varies with the time of day) the 11.9° field of view at 74 MHz corresponds to a patch of sky roughly 100-200 km in diameter. Very large scale variations (≥ 1000 km) in the TEC impose a linear phase gradient across the field of view which causes all sources to shift, in unison, as a function of time. This time-varying position wander causes smearing of sources, lowering their peak flux. Somewhat smaller ionospheric structure (≥ 100 km) produces phase gradients that are not constant across the field of view. This introduces differential refractive effects, in which pairs of sources no longer wander in unison. Finally, much smaller scale

structures (smaller than the size of the array, or $\geq 10\text{km}$) generate source distortions which are no longer simple phase shifts. These combined effects can cause individual source peaks to be lowered below the noise level and remain undetected. The effects are somewhat analogous to the “seeing” effect in optical telescopes. At 74 MHz the refractive effects can shift objects by more than an arcminute on a scale of tens of minutes (and just a few minutes during particularly bad periods). With our A-array resolution of $30''$, this is a serious problem.

Phase-calibration can solve certain aspects of this problem by removing the first order refractive effect. A model of the field can be made from a very short snapshot observation. The time interval of the snapshot should be a time period too short for the source-wander to be significant, generally about one minute. Phase-only self-calibration of all the data to this model will align the source positions at all times to that of the snapshot. Though there will still be a source location offset, it will be constant in time removing the smear and restoring the original morphology and peak flux.

The limitation of this technique is that the ionospheric phase offsets vary across the 11.9° primary beam, producing different position shifts in different regions. However, standard self-calibration does not compensate for the higher order refractive effects that cause differential refraction and higher order source distortions. This is why adding sources other than 3C63 to our self-calibration model did not improve the images. Though the position of 3C63 was fixed, the positions of other sources in the field were not. Figure 2 shows the position offsets as a function of time for six bright sources in the field. These position offsets are measured relative to the expected position of the sources relative to 3C63. This plot shows that the source locations “wander” over the course of the observation, sometimes by more than $2'$. Table 1 shows the RMS offsets for each source in Figure 2 during two time intervals. The first time interval is the first 200 minutes of the observation during which the ionosphere was very active. The second time interval consists of the remainder of the observation, when the ionosphere was relatively “quiet”. The average offsets are drastically different for each time interval. It is also clear that in most cases, the average offsets are greater in sources which are farther away from 3C63. This makes sense as one would expect the applicability of the 3C63-based calibration to decrease with increasing distance from 3C63. This is also seen in an image produced from the self-calibrated data set of the entire primary beam (Figure 3, left). Here, the density of sources visibly decreases with increasing distance from 3C63 as the ionospheric smearing causes the source peaks to decrease. (Primary beam attenuation causes the source density to fall off toward the field edges as well.)

Recently, J. Condon and W. D. Cotton of NRAO developed an imaging algorithm to apply the position-dependent calibration needed to correct for the higher order refractive effects across the full primary beam (Cotton & Condon 2002). Implemented in the AIPS

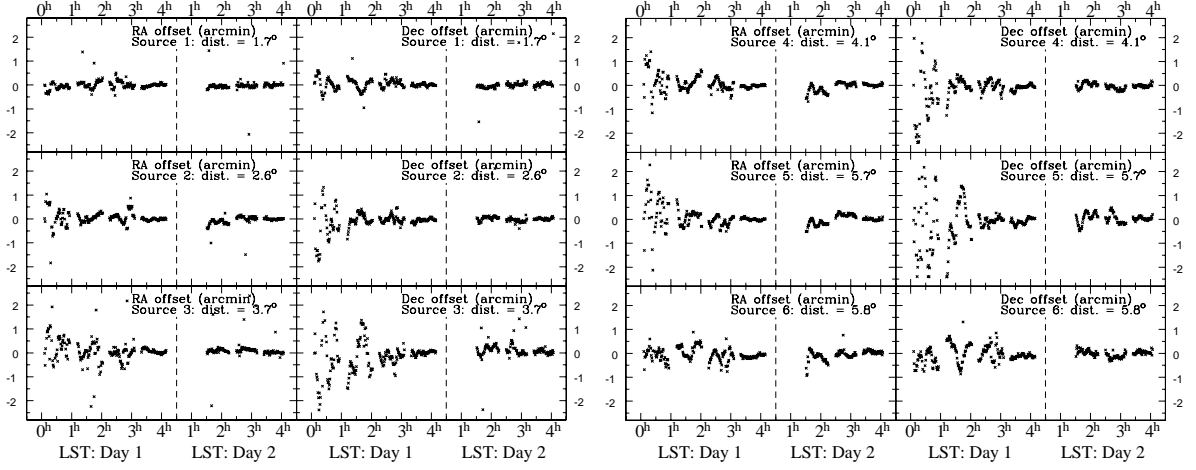


Fig. 2.— The movement of various sources in the primary beam relative to 3C63. The distance of each source from 3C63 is labeled. It seems clear that the closest source, at a distance of 1.7° , moves less with respect to 3C63 than do sources farther away. The “seeing” due to the ionosphere appears to vary greatly in time as well.

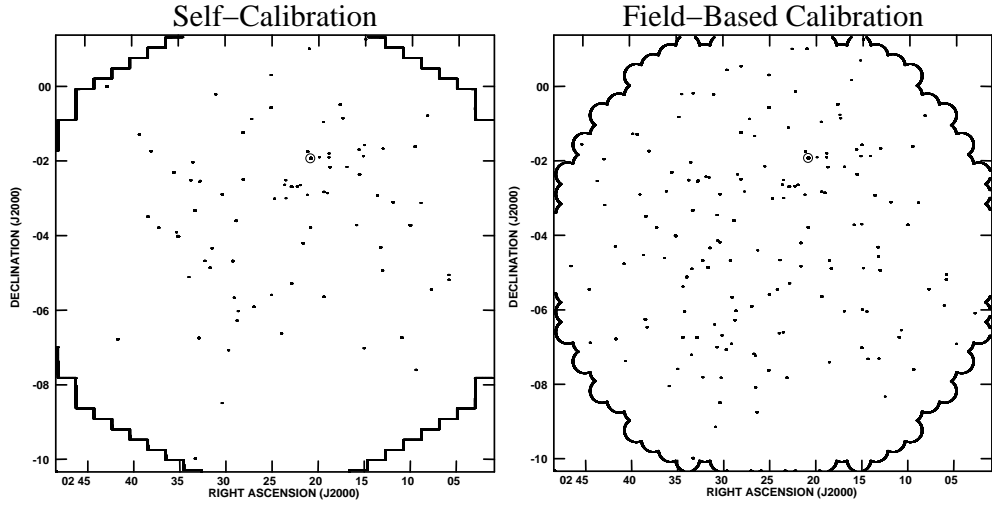


Fig. 3.— Images of the 74 MHz primary beam area produced using self-calibration (left) and VLA FM (right). The bright source 3C63 is circled. This is a contour map in which the first contour is set so far above the noise, 400 mJy/beam, that only actual sources appear. Since the synthesized beam is so small compared to the entire field, the sources simply appear as dots at this scale.

task VLAFM (VLA-Four-Meter), it produces images of facets placed at the locations of the brightest sources known from the NVSS catalog to be in the field. For each observation time interval the position of the source with respect to its known position is measured. The time interval is chosen to be small enough that the source wander over that time is negligible, which in our experience is generally one or two minutes. Based on the source shifts as a function of position in the sky, a 2^{nd} order Zernike polynomial model of the ionosphere is produced for each time interval. Typically not many more than about 6 sources in a given field are bright enough for their positions to be accurately measured in such a short time interval with the VLA, and it is this that sets the limit to the order of Zernike polynomial that VLAFM was designed to fit. When mapping the field, this model of the ionosphere is used to apply a different phase calibration to each facet of the image. Deconvolution is performed by subtracting the clean components from the uv data, after reversing the ionospheric corrections, and remapping the field with the ionospheric corrections restored.

We applied VLAFM to our self-calibrated data set with striking results in the resulting image (Figure 3). With position-dependent phase calibration, the source density becomes uniform across the field, with many more sources detected. It is clear that VLAFM greatly improved the ionospheric distortions in the image. Distortions from the smallest scale (< 10 km) ionospheric structures demand higher order Zernike terms or alternative algorithms. Ignoring them ultimately limits our image fidelity; efforts to develop solutions to this challenge are ongoing.

3.3.2. *Final 74 MHz Image*

We use the image produced with VLAFM as our final image. We used a circular restoring beam with $\text{FWHM} = 30''$, and the pixel spacing was $7.5''$. We set the facet size to 360 pixels and we needed 349 facets to cover the primary beam area. Another 11 facets outside of the primary beam area were included because the NVSS catalog indicated they contained bright outlier sources. With the facets combined, the entire field is 5600 pixels on a side. As with the 325 MHz image, we corrected the primary beam attenuation away from the field center by dividing by the primary beam pattern with the AIPS task PBCOR. This resulted in somewhat higher noise toward the field edges.

4. Source Extraction

With millions of pixels and hundreds of sources, we needed an automated and consistent method for locating and characterizing sources in the maps. The algorithm we used is the AIPS task VSAD, which was produced for use in the NVSS survey (Condon et al. 1998). This task searches the field for islands of emission with peak flux density greater than some specified cutoff level, and then fits the island with a model composed of multiple Gaussian components, with each parameterized by central position, peak flux density, major and minor axes and position angle.

To distinguish “real” sources from noise, we first determined the root mean square noise (σ_{rms}) of the image. This was measured for the central region of each image with the AIPS task IMEAN. We then set the peak flux cutoff in VSAD at the $5\sigma_{rms}$ level. Additionally, we required that the *integrated* flux of each source, calculated as the peak flux density per beam times the Gaussian area in units of beamsize, also be greater than $5\sigma_{rms}$. Sidelobes from very bright sources could be confused as sources. Therefore, we removed sources with peak flux less than 0.04 times that of a nearby source. Smearing effects, such as from bandwidth and time averaging as well as from inaccurately removed ionospheric refraction, can lower the peak flux density of a source. However, if the ionospheric effects are primarily refractive this flux is not lost, but merely spread out. Therefore, we regard the integrated flux, calculated as the peak flux density per beam times the Gaussian area in beams, as the more robust flux density measurement, particularly at 74 MHz, and we use this for the remainder of the paper.

5. Results

5.1. 325 MHz Results

With the criteria of Section 4, we detect 256 sources at 325 MHz. Of these, 219 were single (“S”) sources and 37 were multiple (“M”) sources. (Multiple sources were defined as any sources that were closer together than $60''$.) We classify as “unresolved” those sources in which the major axis of the Gaussian fit was indistinguishable from the beam size at the 2σ level. Of the 219 single component sources, 116 were unresolved. A size distribution histogram for all 256 sources is shown in Figure 4. Images of several of the larger resolved sources are shown in Figure 10, and we present our complete catalog in Table 2. With this many sources, some statistics about radio sources at this frequency and flux density limit can be determined.

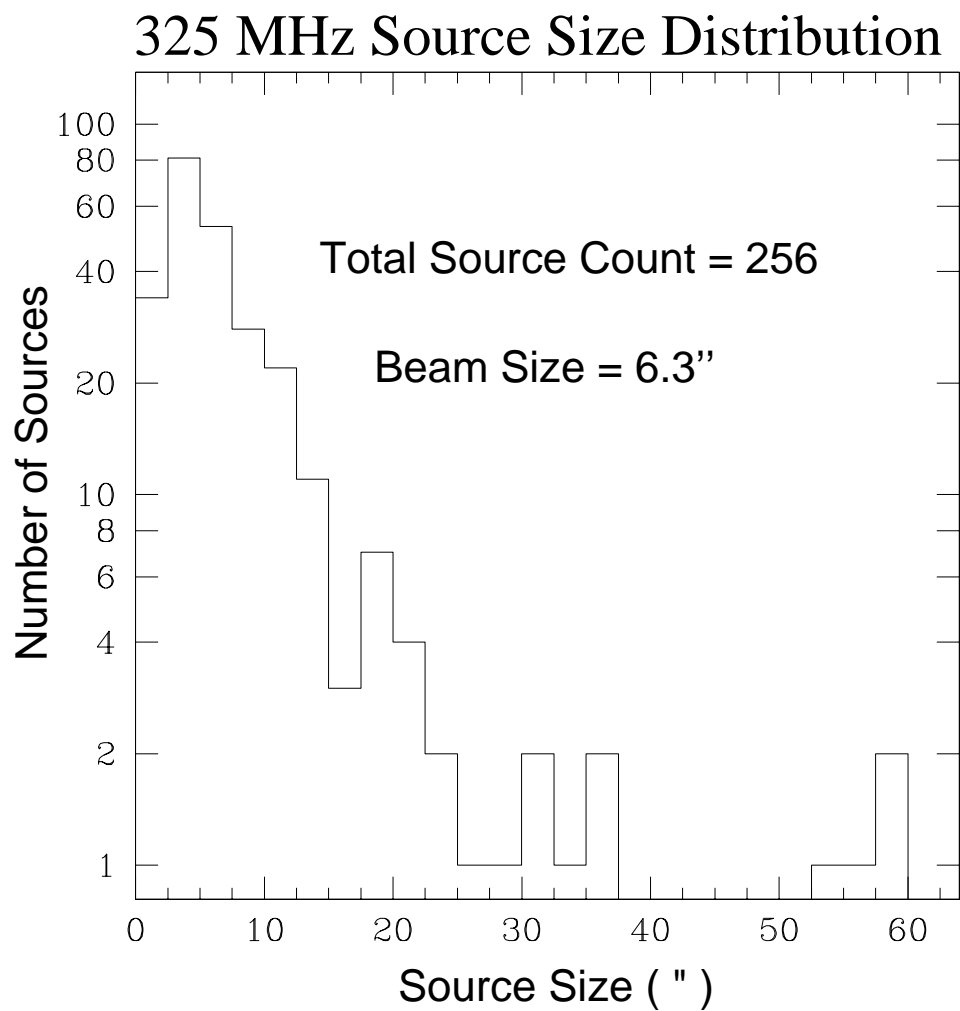


Fig. 4.— Histograms of the deconvolved source size distribution for the 325 MHz survey. Source size plotted is either the major axis of the fitted Gaussian for the single sources or the largest source separation for the multiple sources.

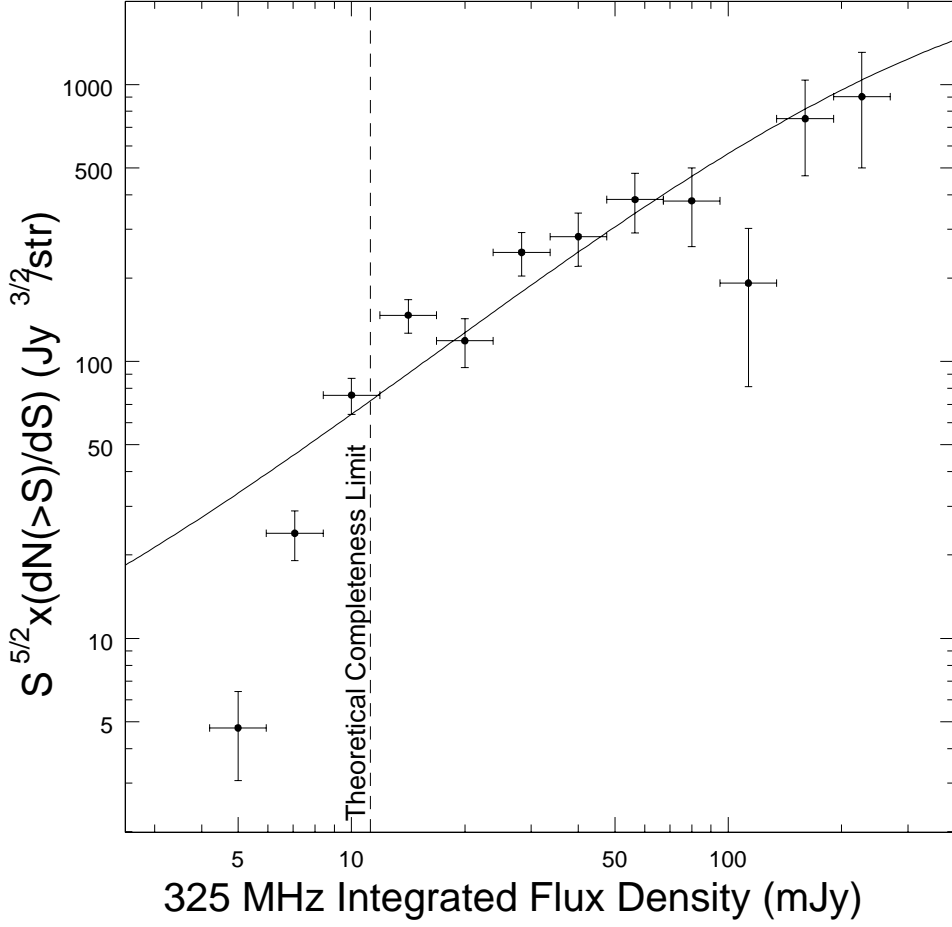


Fig. 5.— Euclidean normalized differential source counts for the 325 MHz image. Also plotted is the curve showing the source counts from a deep WSRT survey (Wieringa 1991).

In Figure 5, we show the Euclidean normalized differential source counts. The source density is calculated as the number of sources detected in each flux bin, divided by the solid angle of the full field of view. The completeness level shown is that for the field edge, where the noise is highest. For this plot, we are limited on the low-flux density side by the flux density limit of our observation, and on the high-flux density side by the relatively small area of our survey. Therefore, compared to the WENSS measurement of the differential source count (Rengelink, et al. 1997), which had a much larger survey region but higher limiting flux density, we measured a very different region of this curve, though there is some overlap. The curve on the plot is a polynomial fit to the differential source count from a deep Westerbork survey (Wieringa 1991). In general, we find close agreement between their results and our own. However, there is possibly a trend with our source counts being slightly higher at lower flux densities, and slightly lower at higher flux densities. If real, this could possibly be explained by the fact that our resolution was nearly an order of magnitude higher. Therefore, some of the extended emission from the bright sources could have been resolved out of our observations. This would result in some bright sources at low resolution being counted as faint sources at high resolution.

We compared our source list to the NVSS catalog, searching for counterpart sources within $45''$ of each of our sources. We found NVSS counterparts to 181 out of 256 sources. The remaining 75 sources most likely have 1.4 GHz fluxes below the NVSS sensitivity limit of 2.5 mJy/beam, and we can calculate the upper limits to their spectral indices. Most of the spectral index upper limits seems quite reasonable, although a handful require quite steep spectra ranging down to as low as $\alpha = -1.56$. In Figure 6 we plot the spectral indices (α_{325}^{1400}) of all the sources with counterparts in NVSS. The difference in resolution ($\sim 6''$ in our map, $45''$ for NVSS) between our data and NVSS means that for extended sources, we may miss some of the 325 MHz flux and so estimate the spectral index to be flatter than it truly is. The median spectral index was $\alpha_{325}^{1400} = -0.87$ (this includes upper limits for sources with no NVSS counterpart). There are six sources with inverted spectra ($\alpha_{325}^{1400} > 0$), though we would need matched resolution to verify this. Seven steep-spectrum sources ($\alpha_{325}^{1400} < -1.3$) were revealed, three with measured spectra and four with spectral limits. As our spectral index estimate is, if inaccurate, certainly an overestimate of α , we are confident that these are indeed steep-spectrum objects.

5.2. 74 MHz Results

With the criteria of Section 4, we detect 211 sources at 74 MHz. Of these, 196 were single (“S”) sources and 15 were multiple (“M”) sources. (Multiple sources were defined as

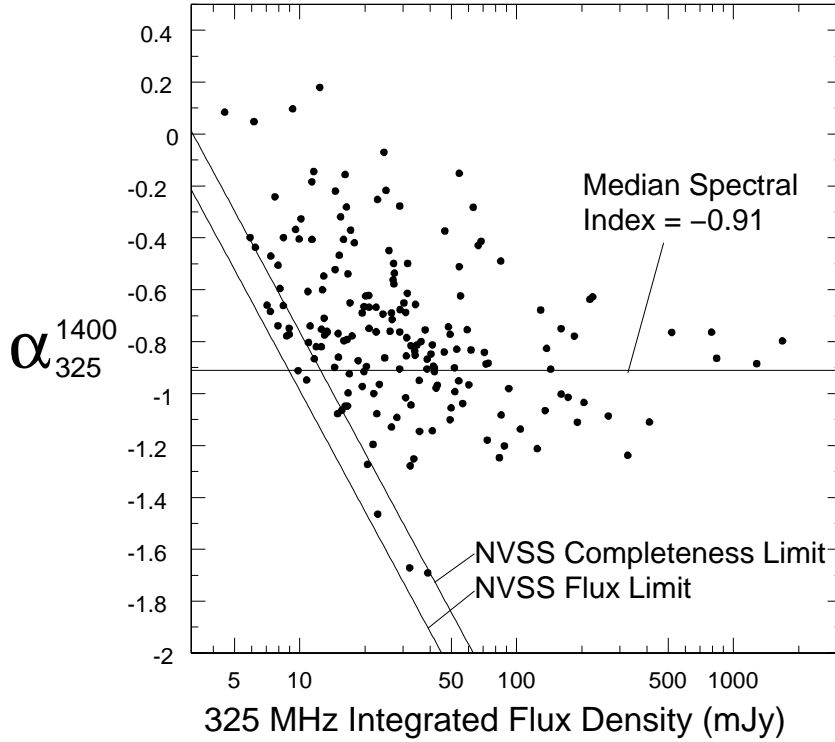


Fig. 6.— Spectral indices (α where $S \propto \nu^\alpha$) from comparing the 325 MHz integrated flux density to the NVSS flux density plotted versus the 325 MHz integrated flux density. The limiting flux density and completeness level of NVSS restrict the parameter space somewhat. Because the 325 MHz image has much greater resolution, the spectral index could be overestimated for resolved sources.

any sources that were closer together than $60''$.) As with the 325 MHz data, we classify as “unresolved” those sources in which the major axis of the Gaussian fit is indistinguishable from the beam size at the 2σ level. Of the 196 single sources, 170 were unresolved, though as we discuss below, the size measurements at 74 MHz have very high uncertainties. Figure 11 shows images of a sample of some of the larger single sources and multiple sources in the field. We present our complete catalog in Table 3.

We plot the Euclidean normalized source count for 74 MHz sources (Figure 7). The completeness level shown is that for the field edge. With no published surveys at 74 MHz, there are no observationally determined source counts with which we can compare these results as we did for our 325 MHz source counts. However, one can adjust the 325 MHz source count curve to 74 MHz by assuming a constant spectral index of sources. This was done for several spectral indices ranging from 0 to -1 , and these curves are also plotted on Figure 7. Comparing these curves to our measured source counts shows that a relatively flat average spectral index of $\alpha_{74}^{325} \sim -0.5$ seems to be most consistent with the data. We caution however, that source counts can be misleading in determining the average spectral index because some fraction of sources become completely absorbed between 325 MHz and 74 MHz.

The 74 MHz resolution ($30''$) is a much closer match to that of NVSS ($45''$), and so we expect to derive accurate spectral indices based on these comparisons. Unlike at 325 MHz, the flux density limit at 74 MHz is so high that we expect all detectable sources to have NVSS counterparts. In fact each 74 MHz source had an NVSS counterpart within $60''$. We plot the spectral index of all 74 MHz sources based on comparisons to the NVSS in Figure 8. We found a median spectral index of $\alpha_{74}^{1400} = -0.72$. This is significantly flatter than the median spectral index for the 325 MHz sources, indicating that in general, source spectra flatten at low frequencies. This result is expected because of absorption effects as well as spectral aging.

Interestingly, in Figure 8, we see no 74 MHz sources with inverted spectra as measured from 1.4 GHz, while we found six in our 325 MHz survey (Figure 6). This seems likely to be a selection effect. Assuming that inverted spectra occur because of synchrotron self-absorption, the flux is expected to decrease dramatically ($S \propto \nu^{5/2}$) below the frequency at which self-absorption becomes significant. Since our source population consists of objects which are relatively bright at 74 MHz, objects with inverted spectra, like gigahertz peaked sources, are simply too faint to be detected, and never enter the sample. The bright source population at 74 MHz is therefore dominated by larger objects like the lobes of radio galaxies which are not noticeably affected by synchrotron self-absorption.

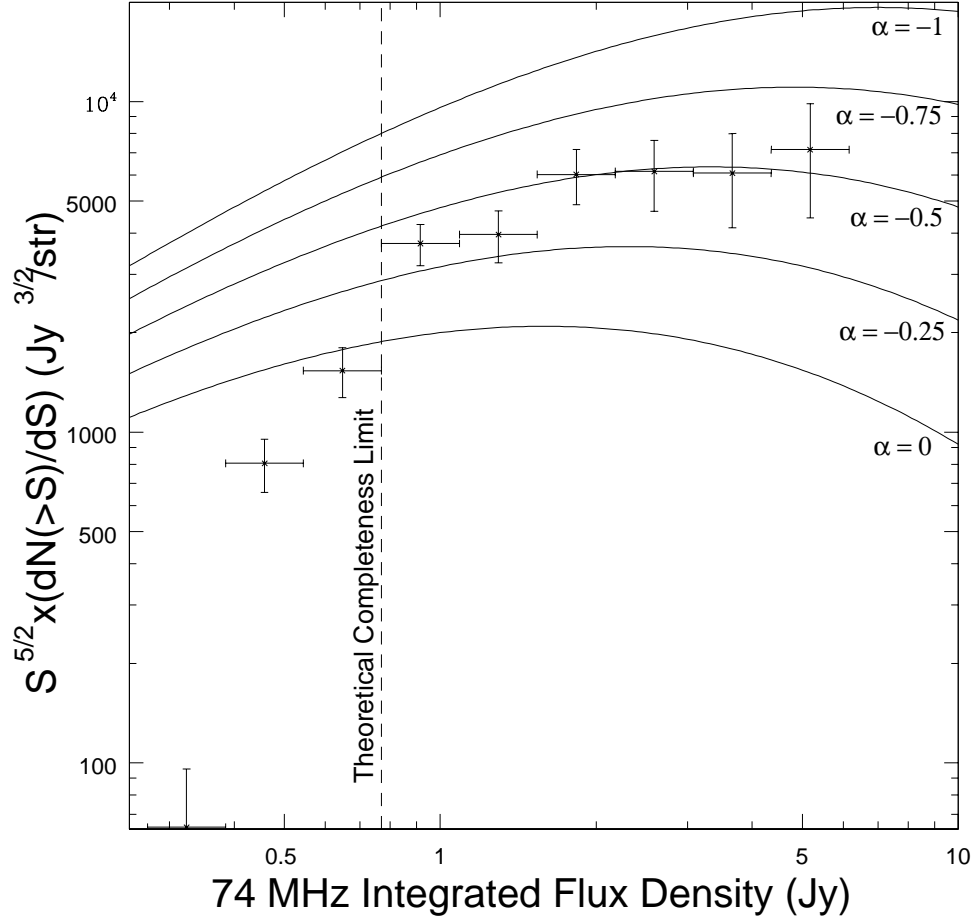


Fig. 7.— Euclidean normalized differential source counts for the 74 MHz image. Also plotted are curves showing the source counts from a deep WSRT survey (Wieringa 1991) scaled to 74 MHz using various spectral indices as labeled.

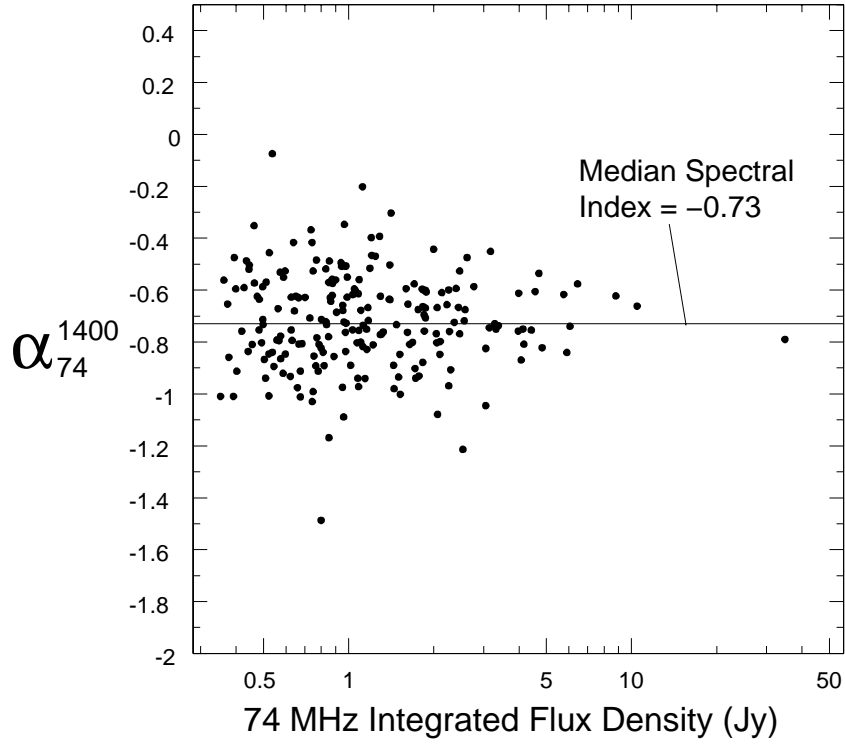


Fig. 8.— Spectral indices (α where $S \propto \nu^\alpha$) from comparing the 74 MHz integrated flux density to the NVSS flux density plotted versus the 74 MHz integrated flux density. The 74 MHz resolution of $30''$ roughly matches the NVSS resolution of $45''$.

5.3. Source Identifications from Literature

Several sources we detected are described in the literature, many of which have optical identifications and redshift measurements. We made use of the NASA/IPAC Extragalactic Database (NED, The NED Team (1992)) to search for published descriptions of all the objects we detected at both frequencies. We classified as an identification any object within $6''$ of our source detection, or within $3'$ for galaxy clusters. In Table 4, we list the 22 objects which have been identified optically as either a galaxy or QSO, and which also have had their redshifts determined. Of these 22 objects, all were detected at 74 MHz, yet only one, J0228.8-0337, was identified at 325 MHz as well. This is likely a selection effect, as our 74 MHz catalog consists of much brighter objects than our 325 MHz catalog. We found that one object, J0238.3-0616, is only $1.6'$ from the known cluster Abell 362 (Abell, Corwin, & Olowin 1989). We detected this object at 74 MHz as one of the largest extended objects at that frequency (seen in Figure 11).

One would expect radio sources detected at 74 MHz to have higher redshifts on average than those detected at higher frequencies. This is because of the steep spectrum nature of high redshift radio galaxies, as well as the tendency for near-by compact radio sources to become synchrotron self-absorbed and not detected at 74 MHz. The median redshift for these 22 objects was $z = 0.8$. This is roughly consistent with the median redshifts found in studies of sources at 1.4 GHz (Waddington, Dunlop, Peacock, & Windhorst 2001). However, 18% (4 out of 22) have redshift above $z > 2$, which is well above the roughly 9% found by Waddington, Dunlop, Peacock, & Windhorst (2001). Further, these 22 objects with redshift in the literature do not constitute a complete sample, and could have a selection bias in favor of low redshift objects redshift. Therefore, these findings seem consistent with 74 MHz sources having higher average redshifts than higher frequency source populations, though further study of a complete sample is necessary to confirm this.

6. Accuracy of Results

The most relevant data we seek to extract from this survey are the positions and fluxes of all detectable sources. We also present source sizes, but as we discuss, these are compromised at 74 MHz by residual ionospheric effects. In this section we discuss the accuracy of these measurements.

The measurement error for each source parameter is a combination of two types of effects, one noise dependent and the other noise independent. The noise dependent error relates to source fitting errors due to map noise, and these naturally decrease with increasing signal

to noise ratio. We calculate these according to the method described by Condon (1997), equations 21, 41 and 42. Noise independent errors are independent of the signal to noise ratio, and include calibration errors and, for 74 MHz, residual ionospheric errors. These errors are discussed in the following sections.

6.1. Noise-Independent Position Errors

For both 325 MHz and 74 MHz observations, the phase calibration is referenced to the NVSS catalog. Therefore, one portion of the noise-independent error is the NVSS calibration uncertainty values of $C_\alpha = 0.45''$ and $C_\delta = 0.56''$ for the right ascension and declination axes respectively (Condon et al. 1998).

For the 74 MHz, observations, this is not the only component of the noise independent error. Another component is the error introduced by incompletely removed ionospheric shifts. As the ionosphere in the field of view was approximated by only a 2^{nd} order Zernike polynomial, there could be residual shifts to source positions. This effect was examined by comparing source positions to the positions of NVSS counterparts (Figure 9). Although the NVSS resolution of $45''$ is somewhat worse than the $30''$ resolution of our 74 MHz image, virtually all NVSS sources are detected at a signal-to-noise ratio at least an order of magnitude greater than at 74 MHz. Therefore, we assume that the NVSS position errors are negligible compared to those of our image, and the position offset of our source from its NVSS counterpart is very close to its actual position measurement error. The rms values of the position offsets, $3.0''$ and $2.5''$ for right ascension and declination respectively, were higher than one would expect with no residual ionospheric shifts. Adding to the position error estimates a constant ionospheric error of $1.7''$ and $1.4''$ for right ascension and declination respectively brought the estimated errors into agreement with those measured with respect to the NVSS. We therefore add in quadrature these values to the noise based position errors in calculating the total position errors.

6.2. Noise-Independent Flux Density Errors

The noise-independent component of the flux density errors consists of the flux density scale uncertainty. The overall flux density scale was set using Cygnus A for 74 MHz and 3C48 for 325 MHz, and this is known to be reliable to 5% accuracy for each frequency (Kassim et al. 2002). Therefore an additional 5% error is added in quadrature to the map noise based source fitting error (Condon 1997).

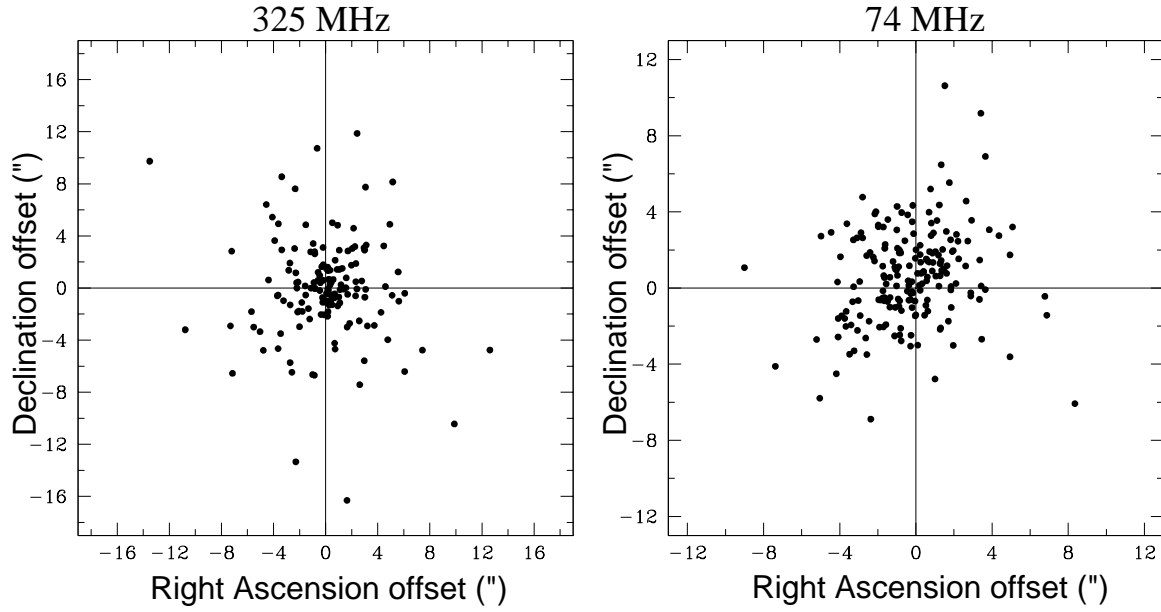


Fig. 9.— Plots of position offsets with respect to NVSS counterparts. All single sources with NVSS counterparts are plotted: 153 and 196 sources for 325 MHz and 74 MHz respectively. The 325 MHz offsets are dominated by NVSS position errors, while the 74 MHz offsets are dominated by 74 MHz position offsets. As the NVSS sources corresponding to 325 MHz sources are much fainter than those corresponding to 74 MHz sources, the position errors are much larger.

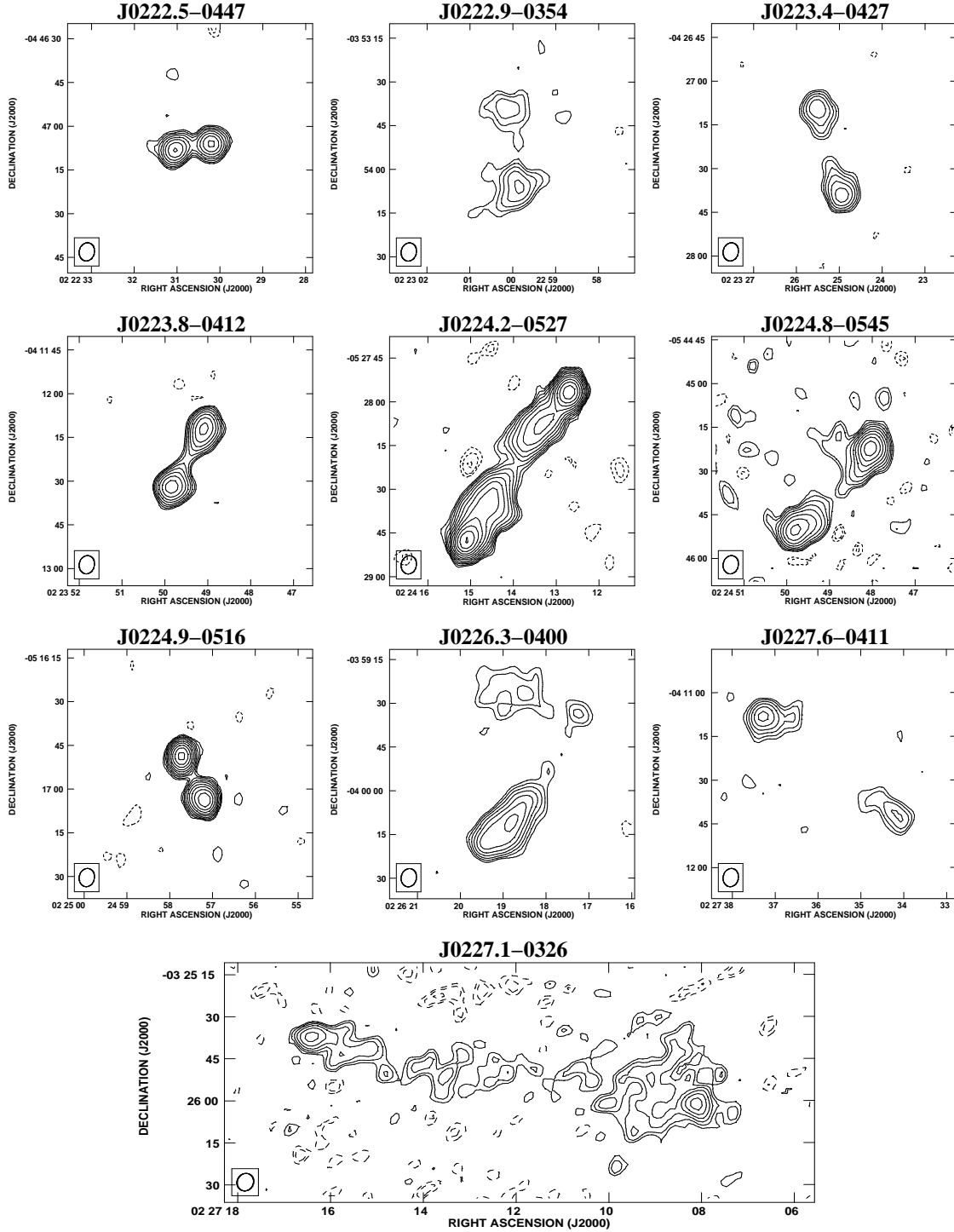


Fig. 10.— A sample of some of the larger resolved sources from the 325 MHz observation. The angular scale is the same in each image. Contour levels are at $2.5 \text{ mJy/beam} \times (-2, -1.4, -1, 1, 1.4, 2, 2.8, 4, 5.8, 8, \dots)$ for each image.

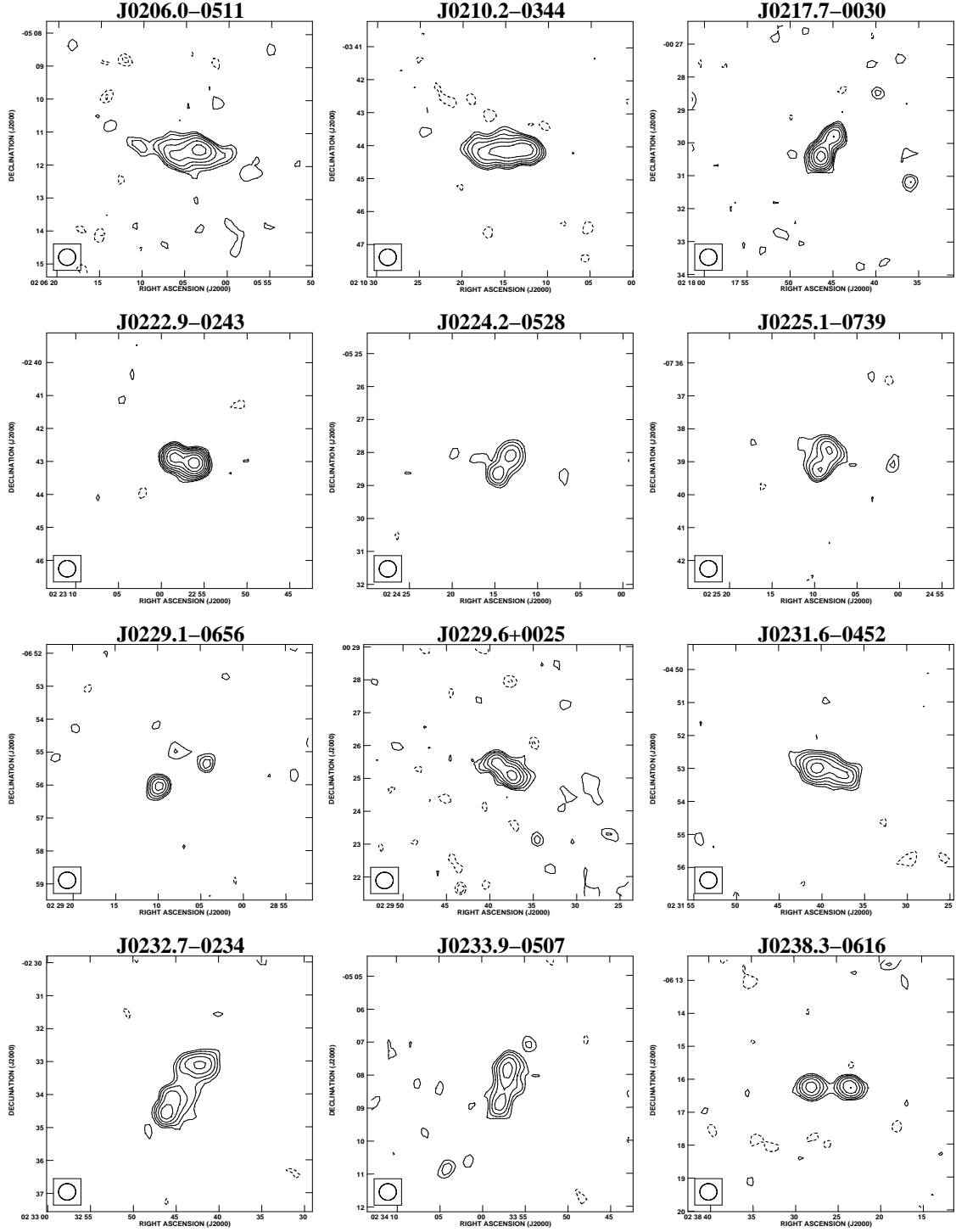


Fig. 11.— A sample of some of the resolved sources from the 74 MHz observation. The angular scale is the same in each image. Contour levels are at $150 \text{ mJy/beam} \times (-2, -1.4, -1, 1, 1.4, 2, 2.8, 4, 5.8, 8, \dots)$.

6.3. Noise-Independent Source Size Errors

At 74 MHz, in addition to the source size uncertainties due to fitting errors, we also must consider residual ionospheric effects. Incompletely removed ionospheric shifts for each time interval combine to smear sources in the final image. This is somewhat analogous to the “seeing” in optical images, and will cause source sizes to be overestimated. It is therefore desirable to measure the amount of “seeing” in an image to remove its effect from source size measurements. For this discussion, we quantify the seeing, θ_{seeing} , as the FWHM of point source imaged with that level of seeing. If we measure a fitted source size of θ_{fit} , and call our beam size θ_{beam} , then we can calculate the deconvolved source size, θ_{source} to be:

$$\theta_{source}^2 = \theta_{fit}^2 - \theta_{beam}^2 - \theta_{seeing}^2 \quad (1)$$

Unfortunately, there is no straightforward way to directly measure the ionospheric “seeing” in an image. This is because of the difficulty in separating seeing effects from actual source sizes. One could consider using, when available, higher resolution images at higher frequencies to determine the actual source sizes to isolate the seeing effect. However, this approach has problems. First of all, sources may not have the same size at 74 MHz, as they do at higher frequencies. For example, a core-lobe source with a flat spectrum core and a steep spectrum lobe could look very different at 74 MHz and at 325 MHz or 1.4 GHz. Further, higher resolution images can resolve out exactly the diffuse emission that 74 MHz is actually biased toward. We therefore discuss two imperfect ways to measure the seeing, and our attempt to make due with this.

The first method for measuring seeing is based on the quality of fitting ionospheric corrections to source offsets during data reduction. In each time interval, the rms offsets of sources from the fitted ionospheric corrections can be calculated. For our 74 MHz data, this method estimates a seeing effect with FWHM of 10.3″. This is likely an overestimate because this figure includes fitting errors and the actual offsets of source centroids between 1.4 GHz and 74 MHz.

Another method is to look at the median source size for all sources in the field. The median is used to reduce the effect of the small number of source which are truly large objects. Taking all single sources, we find the median value for the major axis to be 37.9″. Deconvolving the 30″ restoring beam implies a seeing FWHM of 23.2″. This is also clearly an overestimate, as many sources can be expected to have actual source sizes in this range. In fact, it is likely that our very low frequency biases us toward large objects.

Without a clear way to isolate the ionospheric seeing, we must settle on reasonable

limits to its value. The FWHM value of $23.2''$ derived from fitted source sizes is a safe upper limit. Being extra cautious, we take the lower limit to be 0. We then use Equation 1, and apply the fitting errors on θ_{fit} (Condon 1997) and the upper and lower limits to θ_{seeing} to calculate an upper and lower estimate to θ_{source} . We take the best estimate for θ_{source} to be the average of the upper and lower estimates, and the error to be half the difference. In this way, although we lack a definitive seeing measurement, the error bars on our source sizes encompass all reasonable values. It is also worth noting that for sources much larger than the restoring beam, the seeing adjustments are negligible. Only for sources with sizes of order the beam size or smaller do the seeing adjustments make a significant difference. Efforts are continuing to devise an accurate way to measure the seeing effect in 74 MHz images.

7. Completeness

Since our detection threshold is $5\sigma_{rms}$, and 95% of sources will be measured to within $2\sigma_{rms}$, a reasonable estimate of the completeness level is $7\sigma_{rms}$. Of course the noise level varies over the field because we divided the map by the primary beam pattern to correct for its attenuation of sources. Therefore, no single completeness level can apply to the entire maps. The map noise, σ_{rms} , rises from the field center to the edge, increasing from 0.8 mJy/beam to 1.6 mJy/beam at 325 MHz and from 55 mJy/beam to 110 mJy/beam at 74 MHz. For the entire field, we can say we are complete at the 11.2 mJy and 770 mJy levels at 325 and 74 MHz respectively, though these levels fall to 5.6 mJy and 385 mJy for the inner regions of the fields. That our measurements are consistent with the results of a previous survey (Wieringa 1991) indicates that the theoretical values for completeness levels are reasonable.

8. Conclusions and Future Work

We have successfully surveyed the XMM-LSS region partially at 325 MHz and completely at 74 MHz, detecting 256 and 211 objects respectively. We demonstrated that the full primary beam can be accurately imaged at sub-arcminute resolution at 74 MHz if ionospheric effects are numerically removed. Realization of most of the scientific goals of this survey awaits comparison with upcoming optical and X-ray data from this field. However, the radio data alone have provided useful insight into the low-frequency radio source population, particularly at 74 MHz which has not previously been explored. In the future we hope to perform a more thorough survey of the XMM-LSS region, surveying a larger area at 325 MHz and to a deeper flux limit at 74 MHz. This will dramatically increase the number of

radio sources we detect in this field, improving our ability to relate the nature and location of extra-galactic radio sources to the environment they inhabit in the large scale structure of the universe.

9. Acknowledgments

The authors made use of the database CATS (Verkhodanov 1997) of the Special Astrophysical Observatory. This research has made use of the NASA/IPAC Extragalactic Database (NED) which is operated by the Jet Propulsion Laboratory, Caltech, under contract with the National Aeronautics and Space Administration. Basic research in radio astronomy at the Naval Research Laboratory is supported by the office of Naval Research.

REFERENCES

- Abell, G. O., Corwin, H. G., & Olowin, R. P. 1989, *ApJS*, 70, 1
- Arnaud, M. & Evrard, A. E. 1999, *MNRAS*, 305, 631
- Baars, J. W. M., Genzel, R., Pauliny-Toth, I. I. K., & Witzel, A. 1977, *A&A*, 61, 99
- Becker, R. H. et al. 2001, *ApJS*, 135, 227
- Clark, B. G. 1980, *A&A*, 89, 377
- Condon, J. J. 1997, *PASP*, 109, 166
- Condon, J. J., Cotton, W. D., Greisen, E. W., Yin, Q. F., Perley, R. A., Taylor, G. B., & Broderick, J. J. 1998, *AJ*, 115, 1693
- Cotton, W. D. & Condon, J. J. 2002, *URSI General Assembly*, 17-24 August, 2002, Maastricht, The Netherlands, paper 0944, pp 1-4.
- Douglas, J. N., Bash, F. N., Bozayan, F. A., Torrence, G. W., & Wolfe, C. 1996, *AJ*, 111, 1945
- Drinkwater, M. J. et al. 1997, *MNRAS*, 284, 85
- Dunlop, J. S., Peacock, J. A., Savage, A., Lilly, S. J., Heasley, J. N., & Simon, A. J. B. 1989, *MNRAS*, 238, 1171
- Hales, S. E. G., Baldwin, J. E., & Warner, P. J. 1988, *MNRAS*, 234, 919

- Hewitt, A. & Burbidge, G. 1991, *ApJS*, 75, 297
- Högbom, J. A. 1974, *A&AS*, 15, 417
- Huchra, J. P., Vogeley, M. S., & Geller, M. J. 1999, *ApJS*, 121, 287
- Kassim, N. E., Perley, R. A., & Erickson, W. C. 1991, *ASP Conf. Ser.* 19: IAU Colloq. 131: Radio Interferometry. Theory, Techniques, and Applications, 249
- Kassim, N. E., Perley, R. A., Erickson, W. C., & Dwarakanath, K. S. 1993, *AJ*, 106, 2218
- Kassim, N. E., Lazio, T. J. W., Erickson, W. C., Perley, R. A., Cotton, W. D., Greisen, E. W., Hicks, B., Cohen, A. S., Lane, W. M., & Rickard, L. J. 2002, “The 74 MHz System on the Very Large Array”, (in prep)
- The NED Team, 1992 vol. Report p. 1, REDSHIFT OBTAINED FROM LITERATURE BY THE NED TEAM PRIOR TO NOVEMBER 1992
- Osmer, P. S., Porter, A. C., & Green, R. F. 1994, *ApJ*, 436, 678
- Owen, F. N., Ledlow, M. J., & Keel, W. C. 1995, *AJ*, 109, 14
- Perley, R. A. 1999, *ASP Conf. Ser.* 180: Synthesis Imaging in Radio Astronomy II, 383
- Pierre, M., Alloin, D., Altieri, B., Birkinshaw, M., Bremer, M., Böhringer, H., Hjorth, J., Jones, L., Le Fèvre, O., Maccagni, D., McBreen, B., Mellier, Y., Molinari, E., Quintana, H., Röttgering, H., Surdej, J., Vigroux, L., White, S., Lonsdale, C. 2001, *The Messenger*, 105, 32
- Rees, N. 1990, *MNRAS*, 244, 233
- Refregier, A., Valtchanov, I., & Pierre, M. 2002, *A&A*, 390, 1
- Rengelink, R. B., Tang, Y., de Bruyn, A. G., Miley, G. K., Bremer, M. N., Roettgering, H. J. A., & Bremer, M. A. R. 1997, *A&AS*, 124, 259
- Press, W. H. & Schechter, P. 1974, *ApJ*, 187, 425
- Sloan Digital Sky Survey team, 2001, SLOAN DIGITAL SKY SURVEY EARLY RELEASE AS OBTAINED JUNE 5, 2001
- Stanford, S. A., Stern, D., van Breugel, W., & De Breuck, C. 2000, *ApJS*, 131, 185
- Stocke, J. T., Morris, S. L., Gioia, I. M., Maccacaro, T., Schild, R., Wolter, A., Fleming, T. A., & Henry, J. P. 1991, *ApJS*, 76, 813

- Tovmassian, H. M., Chavushyan, V. H., Verkhodanov, O. V., & Tiersch, H. 1999, *ApJ*, 523, 87
- Verkhodanov O. V., Trushkin S. A., Andernach H., Chernenkov V. N. 1997, “Astronomical Data Analysis Software and Systems VI”, *ASP Conference Series*, Vol. 125, P.322-325
- Vessey, S. J. & Green, D. A. 1998, *MNRAS*, 294, 607
- Waddington, I., Dunlop, J. S., Peacock, J. A., & Windhorst, R. A. 2001, *MNRAS*, 328, 882
- Wieringa, M. H. 1991, Ph.D. Thesis, Leiden Univ., 241
- Wieringa, M. H. 1993, *Bulletin d’Information du Centre de Donnees Stellaires*, 43, 17
- Wright, A. & Otrupcek, R. 1990, *PKS Catalog (1990)*, 0

Table 1. Statistical Overview of Ionospheric Refraction

Source #	Source Name	RA (°)	DEC (°)	Dist. to 3C63 (°)	rms offset: RA (″)	First 200 min. DEC (″)	rms offset: RA (″)	Remainder DEC (″)
1	J0225.1–0035	36.284	-0.592	1.7	9.7	13.3	4.0	4.5
2	J0228.8–0337	37.222	-3.627	2.6	17.4	30.0	6.0	4.6
3	J0219.4–0539	34.868	-5.663	3.7	23.2	44.9	4.7	8.8
4	J0235.1–0402	38.779	-4.035	4.1	25.0	44.2	9.4	6.7
5	J0232.8–0645	38.225	-6.765	5.7	32.7	56.1	9.6	11.1
6	not in table	40.670	-0.013	5.8	17.4	24.0	10.8	7.4

Table 2. 325 MHz Source List

Source	α (J2000) (h m s)	σ_α ($''$)	δ (J2000) ($^\circ$ ' $''$)	σ_δ ($''$)	Dist. ($^\circ$)	T.	S_{int} mJy	major ($''$)	Size minor ($''$)	PA ($^\circ$)	α
J0219.5–0418	02 19 35.76	0.5	−04 18 43.5	0.6	1.28	S	29.0 \pm 3.3	\leq 5.1	\leq 3.1	43 \pm 12	−0.68
J0219.7–0453	02 19 45.39	0.7	−04 53 35.7	1.1	1.28	S	25.8 \pm 5.6	10.4 \pm 2.5	\leq 8.9	2 \pm 11	−0.45
J0219.9–0447	02 19 57.34	0.5	−04 47 54.1	0.6	1.21	S	137.6 \pm 7.6	5.6 \pm 0.2	\leq 1.5	1 \pm 1	−0.83
J0220.2–0421	02 20 13.25	0.5	−04 21 48.7	0.7	1.12	S	20.1 \pm 3.1	5.5 \pm 1.3	\leq 4.3	165 \pm 10	−0.62
J0220.4–0442	02 20 27.91	0.6	−04 42 19.5	0.8	1.07	S	9.9 \pm 2.6	\leq 8.8	\leq 5.2	155 \pm 18	< −0.94
J0220.5–0450	02 20 31.91	0.6	−04 50 02.6	0.9	1.08	S	10.7 \pm 2.8	\leq 9.6	\leq 5.1	176 \pm 14	< −0.99
J0220.5–0514	02 20 35.34	0.5	−05 14 00.4	0.6	1.25	S	50.0 \pm 4.0	5.0 \pm 0.6	\leq 2.4	166 \pm 4	−1.06
J0220.6–0408	02 20 36.12	0.7	−04 08 06.1	0.8	1.08	S	9.6 \pm 2.8	\leq 7.9	\leq 7.8	NA	< −0.92
J0220.6–0437	02 20 39.05	0.5	−04 37 28.1	0.6	1.01	M	34.7 \pm 4.4	9.6			−0.81
	02 20 38.68	0.5	−04 37 20.2	0.9	1.01	C	16.1 \pm 3.2	8.7 \pm 2.1	\leq 4.3	174 \pm 5	−0.81
	02 20 39.05	0.5	−04 37 28.1	0.6	1.01	C	18.6 \pm 2.8	5.1 \pm 1.3	\leq 4.3	166 \pm 11	−0.81
J0220.8–0512	02 20 51.64	0.6	−05 12 38.7	0.8	1.19	S	11.6 \pm 2.9	\leq 8.6	\leq 5.0	161 \pm 17	−0.14
J0220.9–0333	02 20 55.48	0.5	−03 33 31.6	0.6	1.32	S	54.4 \pm 4.2	4.4 \pm 0.5	\leq 2.4	169 \pm 5	−0.51
J0220.9–0348*	02 20 55.80	0.5	−03 48 34.4	0.6	1.16	S	410.0 \pm 20.8	4.9 \pm 0.1	4.0 \pm 0.1	167 \pm 2	−1.11
J0220.9–0413	02 20 58.75	0.6	−04 13 22.6	0.7	0.96	S	9.3 \pm 2.3	\leq 7.4	\leq 5.0	178 \pm 25	< −0.90
J0221.0–0500	02 21 02.00	0.6	−05 00 48.3	0.6	1.04	S	18.6 \pm 3.1	6.7 \pm 1.5	\leq 4.5	113 \pm 8	−0.87
J0221.1–0511	02 21 11.02	0.6	−05 11 22.5	0.7	1.11	S	30.8 \pm 4.4	7.1 \pm 1.3	6.4 \pm 1.2	NA	−0.69
J0221.3–0457	02 21 18.44	0.5	−04 57 23.9	0.6	0.95	S	22.8 \pm 2.5	3.5 \pm 0.9	\leq 3.0	152 \pm 11	−0.25
J0221.3–0344	02 21 19.39	0.5	−03 44 41.7	0.6	1.12	S	27.3 \pm 3.3	4.2 \pm 1.0	4.1 \pm 1.0	NA	−0.54
J0221.3–0329	02 21 19.92	0.5	−03 29 07.0	0.7	1.31	S	24.7 \pm 3.7	5.6 \pm 1.3	\leq 3.7	172 \pm 8	−0.86
J0221.4–0424	02 21 24.00	0.5	−04 24 16.2	0.7	0.82	S	15.0 \pm 2.6	6.5 \pm 1.6	\leq 4.4	156 \pm 8	−1.08
J0221.4–0352	02 21 24.35	0.5	−03 52 40.9	0.6	1.02	S	19.4 \pm 2.5	\leq 5.7	\leq 3.4	136 \pm 13	−0.69
J0221.4–0347	02 21 25.58	0.5	−03 47 21.3	0.6	1.08	S	61.7 \pm 3.9	3.6 \pm 0.4	\leq 1.9	178 \pm 5	−0.83
J0221.4–0411	02 21 26.86	1.0	−04 11 56.5	0.8	0.86	M	15.3 \pm 3.5	17.1			< −1.24
	02 21 26.86	1.0	−04 11 56.5	0.8	0.86	C	8.4 \pm 2.6	\leq 13.2	\leq 5.6	118 \pm 11	< −0.83
	02 21 27.92	0.8	−04 12 02.7	0.9	0.85	C	6.9 \pm 2.3	\leq 10.0	\leq 5.8	143 \pm 20	< −0.69
J0221.4–0516	02 21 27.26	0.5	−05 16 11.8	0.6	1.11	S	14.6 \pm 2.4	\leq 4.9	\leq 4.0	2 \pm 45	−0.22
J0221.4–0504	02 21 27.47	0.7	−05 04 02.8	0.8	0.98	S	5.7 \pm 2.0	\leq 6.2	\leq 6.2	NA	< −0.57
J0221.4–0434	02 21 28.19	1.3	−04 34 11.6	0.7	0.80	S	31.0 \pm 4.8	18.7 \pm 3.0	4.7 \pm 1.3	97 \pm 3	−0.85
J0221.5–0415	02 21 30.55	0.7	−04 15 37.3	0.8	0.82	S	7.3 \pm 2.2	\leq 8.9	\leq 5.5	129 \pm 22	< −0.73
J0221.5–0423	02 21 31.55	0.5	−04 23 47.7	0.6	0.79	S	33.9 \pm 2.6	3.6 \pm 0.6	\leq 2.3	168 \pm 7	−0.84
J0221.5–0402	02 21 33.21	0.6	−04 02 21.8	1.0	0.90	S	12.0 \pm 2.8	8.2 \pm 2.4	\leq 4.8	164 \pm 7	< −1.08
J0221.5–0429	02 21 34.42	0.6	−04 29 24.9	2.1	0.77	S	16.2 \pm 3.8	19.1 \pm 5.0	\leq 5.0	180 \pm 3	< −1.28
J0221.5–0518	02 21 35.95	0.5	−05 18 18.4	0.7	1.11	M	41.8 \pm 5.0	7.9			−0.90
	02 21 35.58	0.5	−05 18 24.1	0.8	1.11	C	23.4 \pm 3.7	9.1 \pm 1.6	\leq 4.1	178 \pm 4	−0.90
	02 21 35.95	0.5	−05 18 18.4	0.7	1.11	C	18.4 \pm 3.0	5.5 \pm 1.4	\leq 3.8	2 \pm 8	−0.90
J0221.6–0426	02 21 40.06	0.9	−04 26 54.0	1.1	0.75	S	13.6 \pm 3.4	10.7 \pm 3.0	\leq 7.8	40 \pm 9	< −1.16
J0221.6–0509	02 21 41.42	0.7	−05 09 43.3	0.7	0.99	S	11.4 \pm 2.6	\leq 8.8	\leq 4.7	125 \pm 13	−0.18
J0221.7–0451*	02 21 42.06	0.5	−04 51 13.0	0.6	0.82	S	264.9 \pm 13.5	9.3 \pm 0.1	\leq 1.0	166 \pm 0	−1.09
J0221.7–0413*	02 21 43.10	0.5	−04 13 45.9	0.6	0.78	S	1683.2 \pm 84.2	7.8 \pm 0.0	\leq 0.4	146 \pm 0	−0.80
J0221.7–0357	02 21 44.33	0.5	−03 57 51.3	0.6	0.91	M	42.6 \pm 3.7	19.7			−0.98
	02 21 44.33	0.5	−03 57 51.3	0.6	0.91	C	27.9 \pm 2.7	4.5 \pm 0.8	\leq 3.4	139 \pm 8	−0.98
	02 21 45.51	0.5	−03 57 42.6	0.6	0.90	C	14.7 \pm 2.1	\leq 4.6	\leq 3.6	178 \pm 36	−0.98
J0221.7–0329	02 21 45.64	0.5	−03 29 31.8	0.6	1.24	S	20.5 \pm 3.1	\leq 6.4	\leq 3.7	176 \pm 12	−1.27
J0221.7–0326	02 21 47.74	0.5	−03 26 39.3	0.7	1.28	S	35.7 \pm 5.0	8.9 \pm 1.4	\leq 6.0	155 \pm 6	−1.15
J0221.7–0359	02 21 47.77	0.6	−03 59 27.4	1.0	0.88	S	9.8 \pm 2.7	\leq 12.5	\leq 5.2	2 \pm 9	< −0.93
J0221.8–0356	02 21 48.60	0.7	−03 56 52.4	1.5	0.90	S	13.2 \pm 3.5	12.9 \pm 3.8	\leq 5.0	161 \pm 4	< −1.14
J0221.8–0505	02 21 51.49	0.6	−05 05 39.3	0.8	0.92	S	15.2 \pm 3.0	6.9 \pm 1.8	\leq 5.7	30 \pm 11	−0.47
J0221.8–0427	02 21 51.95	0.6	−04 27 30.7	0.8	0.70	S	8.9 \pm 2.2	\leq 8.5	\leq 5.5	5 \pm 20	−0.75
J0221.9–0428	02 21 54.42	0.7	−04 28 25.3	1.2	0.69	S	9.6 \pm 2.7	\leq 16.0	\leq 5.2	162 \pm 6	< −0.92
J0221.9–0410	02 21 56.24	0.7	−04 10 13.3	1.4	0.76	S	10.0 \pm 2.9	\leq 18.2	\leq 5.4	165 \pm 6	< −0.95
J0221.9–0407	02 21 56.49	0.5	−04 07 58.8	0.6	0.77	S	14.4 \pm 2.2	4.9 \pm 1.3	\leq 3.8	132 \pm 10	< −1.20
J0221.9–0443	02 21 59.84	0.6	−04 43 28.1	0.8	0.70	S	10.1 \pm 2.4	\leq 8.3	\leq 6.9	NA	< −0.95
J0222.0–0339	02 22 00.40	0.5	−03 39 35.5	0.6	1.07	S	71.1 \pm 4.4	3.9 \pm 0.3	2.6 \pm 0.4	151 \pm 8	−0.84
J0222.0–0448	02 22 04.03	0.6	−04 48 36.1	0.7	0.72	S	10.5 \pm 2.2	\leq 8.3	\leq 4.4	154 \pm 12	< −0.98
J0222.0–0338	02 22 04.81	0.5	−03 38 15.8	0.6	1.08	S	129.2 \pm 6.9	4.1 \pm 0.2	\leq 1.3	177 \pm 2	−0.68
J0222.0–0407	02 22 05.18	0.9	−04 07 08.2	1.5	0.75	S	16.2 \pm 4.2	13.3 \pm 3.7	\leq 10.2	160 \pm 10	< −1.28
J0222.1–0334	02 22 06.32	0.5	−03 34 19.7	0.6	1.13	S	31.5 \pm 2.9	\leq 3.9	\leq 2.7	138 \pm 18	−0.50
J0222.1–0428	02 22 08.08	1.1	−04 28 11.6	1.2	0.63	S	16.2 \pm 3.7	14.8 \pm 3.6	\leq 7.1	137 \pm 5	−0.16
J0222.1–0452	02 22 11.68	0.7	−04 52 23.2	0.9	0.72	S	6.8 \pm 2.1	\leq 8.6	\leq 6.4	5 \pm 36	< −0.69
J0222.2–0428	02 22 12.99	0.5	−04 28 35.2	0.6	0.61	S	16.6 \pm 2.2	5.3 \pm 1.1	\leq 3.5	164 \pm 7	−1.05
J0222.3–0453	02 22 22.82	0.5	−04 53 26.7	0.6	0.69	S	15.1 \pm 1.9	\leq 4.7	\leq 3.4	139 \pm 22	−0.86
J0222.4–0407	02 22 27.59	0.6	−04 07 18.7	0.7	0.67	S	12.4 \pm 2.4	5.9 \pm 1.7	\leq 5.8	133 \pm 15	< −1.09
J0222.4–0431	02 22 28.32	0.5	−04 31 23.8	0.6	0.55	M	26.7 \pm 3.0	19.6			−0.71
	02 22 28.32	0.5	−04 31 23.8	0.6	0.55	C	19.1 \pm 2.0	4.1 \pm 0.9	\leq 3.0	178 \pm 9	−0.71
	02 22 28.86	0.6	−04 31 41.7	0.8	0.55	C	7.6 \pm 2.0	\leq 8.9	\leq 5.0	173 \pm 16	−0.71

Table 2—Continued

Source	α (J2000) (h m s)	σ_α ($''$)	δ (J2000) ($^\circ$ ' $''$)	σ_δ ($''$)	Dist. ($^\circ$)	T.	S_{int} mJy	major ($''$)	Size minor ($''$)	PA ($^\circ$)	α
J0222.5–0352	02 22 30.03	0.7	−03 52 37.9	0.7	0.82	S	6.2 ± 1.9	≤ 7.0	≤ 5.7	NA	−0.44
J0222.5–0447	02 22 30.21	0.5	−04 47 06.1	0.6	0.61	M	87.9 ± 5.3	12.5			−1.20
	02 22 30.21	0.5	−04 47 06.1	0.6	0.61	C	44.8 ± 3.0	4.3 ± 0.4	3.1 ± 0.5	158 ± 10	−1.20
	02 22 31.04	0.5	−04 47 08.0	0.6	0.61	C	43.1 ± 3.0	4.7 ± 0.4	2.5 ± 0.5	130 ± 5	−1.20
J0222.7–0535	02 22 42.91	0.7	−05 35 33.8	0.9	1.20	S	8.5 ± 2.9	≤ 9.4	≤ 6.0	26 ± 25	< −0.84
J0222.7–0402	02 22 44.34	0.6	−04 02 35.4	0.8	0.66	S	7.9 ± 2.1	≤ 8.1	≤ 6.0	16 ± 32	−0.74
J0222.7–0348	02 22 47.65	0.5	−03 48 17.2	0.6	0.84	S	51.8 ± 3.3	4.0 ± 0.4	≤ 1.9	167 ± 4	−0.90
J0222.8–0504	02 22 48.47	1.0	−05 04 55.4	1.4	0.74	S	11.8 ± 3.2	13.2 ± 4.0	≤ 5.1	146 ± 4	< −1.06
J0222.8–0412	02 22 48.76	0.5	−04 12 15.9	0.6	0.55	S	13.0 ± 1.8	≤ 4.5	≤ 3.5	173 ± 32	−0.71
J0222.8–0432	02 22 51.17	0.7	−04 32 15.3	0.8	0.45	S	4.5 ± 1.5	≤ 6.0	≤ 6.0	NA	0.08
J0222.8–0416	02 22 52.10	0.5	−04 16 47.7	0.7	0.50	S	13.0 ± 2.0	5.1 ± 1.3	≤ 3.7	179 ± 9	−0.77
J0222.9–0414	02 22 54.71	0.5	−04 14 04.7	0.6	0.51	S	31.4 ± 3.3	7.7 ± 0.9	5.9 ± 0.8	7 ± 13	−0.61
J0222.9–0435	02 22 54.98	0.6	−04 35 08.7	0.7	0.45	S	8.7 ± 1.8	≤ 7.6	≤ 4.5	127 ± 16	−0.78
J0222.9–0518*	02 22 55.77	0.5	−05 18 18.5	0.6	0.91	S	793.2 ± 39.7	4.2 ± 0.0	≤ 0.5	179 ± 0	−0.76
J0222.9–0424	02 22 56.45	0.5	−04 24 50.5	0.6	0.44	S	85.0 ± 4.6	5.2 ± 0.2	≤ 1.4	165 ± 1	−1.08
J0222.9–0407	02 22 58.06	0.6	−04 07 03.6	0.7	0.57	S	11.7 ± 2.1	6.0 ± 1.6	≤ 4.1	137 ± 8	−0.87
J0222.9–0504	02 22 58.25	0.5	−05 04 20.2	0.7	0.71	S	38.6 ± 3.5	11.1 ± 1.0	≤ 3.3	0 ± 2	−0.90
J0222.9–0354	02 22 59.90	0.6	−03 54 06.1	0.7	0.73	M	73.3 ± 7.6	26.8			−1.18
	02 22 59.90	0.6	−03 54 06.1	0.7	0.73	C	41.9 ± 4.8	11.5 ± 1.3	8.0 ± 1.0	164 ± 9	−1.18
	02 23 00.11	0.9	−03 53 39.5	0.9	0.73	C	31.4 ± 5.3	12.7 ± 2.2	10.3 ± 1.8	88 ± 22	−1.18
J0223.0–0409	02 23 01.27	0.5	−04 09 37.5	0.6	0.53	S	10.2 ± 1.8	≤ 5.8	≤ 4.1	177 ± 24	−0.33
J0223.1–0444	02 23 06.70	0.5	−04 44 45.5	0.6	0.46	S	15.9 ± 1.8	≤ 4.6	≤ 3.1	147 ± 18	−0.41
J0223.1–0423	02 23 10.20	0.5	−04 23 07.5	0.6	0.39	S	68.7 ± 3.8	3.8 ± 0.2	≤ 1.5	164 ± 2	−0.41
J0223.2–0458	02 23 16.58	0.6	−04 58 45.6	0.7	0.59	S	9.9 ± 2.0	≤ 6.5	≤ 5.8	NA	< −0.94
J0223.2–0444	02 23 17.12	1.0	−04 44 51.5	1.2	0.42	S	8.4 ± 2.5	≤ 17.0	≤ 5.4	142 ± 6	< −0.83
J0223.3–0445	02 23 19.20	0.7	−04 45 48.8	0.8	0.43	S	12.4 ± 2.4	9.0 ± 2.1	≤ 4.2	140 ± 5	< −1.10
J0223.3–0318	02 23 20.69	0.5	−03 18 25.4	0.6	1.24	S	24.5 ± 2.9	≤ 4.2	≤ 3.3	178 ± 33	−0.07
J0223.3–0501	02 23 22.12	0.6	−05 01 37.5	0.7	0.62	S	7.6 ± 1.9	≤ 8.2	≤ 5.0	144 ± 20	< −0.76
J0223.4–0427	02 23 24.96	0.5	−04 27 38.1	0.6	0.31	M	74.1 ± 5.3	29.1			−0.88
	02 23 24.96	0.5	−04 27 38.1	0.6	0.31	C	40.3 ± 3.3	7.8 ± 0.6	5.5 ± 0.6	16 ± 7	−0.88
	02 23 25.49	0.5	−04 27 10.1	0.6	0.31	C	33.7 ± 3.2	8.6 ± 0.8	5.3 ± 0.7	9 ± 6	−0.88
J0223.4–0540	02 23 27.45	0.5	−05 40 45.1	0.6	1.22	S	26.1 ± 3.0	≤ 4.7	≤ 3.1	148 ± 16	−0.76
J0223.5–0401	02 23 32.36	0.6	−04 01 47.1	0.7	0.55	S	5.9 ± 1.6	≤ 5.3	≤ 5.3	NA	−0.40
J0223.5–0514	02 23 32.41	0.5	−05 14 38.5	0.6	0.80	S	16.7 ± 2.3	4.5 ± 1.1	≤ 3.4	1 ± 10	−1.00
J0223.5–0458	02 23 33.45	2.2	−04 58 31.2	1.8	0.55	S	28.9 ± 4.8	35.0 ± 6.5	≤ 5.6	128 ± 1	−0.28
J0223.5–0453	02 23 33.86	0.9	−04 53 00.3	0.8	0.47	S	6.4 ± 2.0	≤ 10.2	≤ 6.7	112 ± 25	< −0.64
J0223.6–0459	02 23 36.71	0.7	−04 59 25.6	0.7	0.56	S	5.3 ± 1.6	≤ 6.3	≤ 5.7	NA	< −0.52
J0223.6–0536	02 23 36.80	0.8	−05 36 05.9	1.2	1.13	S	11.9 ± 3.6	≤ 15.7	≤ 5.5	150 ± 8	< −1.07
J0223.6–0409	02 23 37.60	0.6	−04 09 36.8	0.7	0.43	M	16.9 ± 2.7	11.6			−0.92
	02 23 36.84	0.6	−04 09 34.0	0.7	0.43	C	9.1 ± 2.0	≤ 9.3	≤ 4.6	145 ± 11	−0.92
	02 23 37.60	0.6	−04 09 36.8	0.7	0.43	C	7.9 ± 1.7	≤ 6.6	≤ 4.6	167 ± 26	−0.92
J0223.6–0506	02 23 38.27	0.6	−05 06 29.0	0.6	0.66	S	34.0 ± 3.4	10.5 ± 1.1	3.2 ± 0.8	104 ± 3	−0.85
J0223.7–0412	02 23 42.84	0.5	−04 12 00.5	0.6	0.38	S	23.3 ± 2.2	5.4 ± 0.7	≤ 2.7	168 ± 4	−0.96
J0223.7–0340	02 23 45.44	0.5	−03 40 42.8	0.6	0.85	S	143.8 ± 7.6	4.8 ± 0.1	3.3 ± 0.2	137 ± 3	−0.91
J0223.7–0332	02 23 46.62	0.5	−03 32 36.6	0.6	0.98	S	160.5 ± 8.3	3.9 ± 0.1	≤ 1.1	156 ± 1	−0.75
J0223.8–0412	02 23 49.82	0.5	−04 12 31.7	0.6	0.36	M	135.5 ± 7.5	21.9			−1.07
	02 23 49.10	0.5	−04 12 12.7	0.6	0.36	C	68.8 ± 4.2	9.1 ± 0.4	2.3 ± 0.4	158 ± 1	−1.07
	02 23 49.82	0.5	−04 12 31.7	0.6	0.36	C	66.7 ± 4.0	7.0 ± 0.3	3.5 ± 0.3	149 ± 2	−1.07
J0223.8–0531	02 23 49.84	0.5	−05 31 05.8	0.6	1.04	S	10.8 ± 2.1	≤ 4.4	≤ 4.4	NA	−0.95
J0223.8–0522	02 23 52.71	0.5	−05 22 26.6	0.6	0.90	S	41.4 ± 2.9	2.4 ± 0.6	≤ 2.1	161 ± 12	−0.89
J0223.9–0441*	02 23 57.10	0.5	−04 41 13.5	0.6	0.26	S	325.6 ± 16.4	4.6 ± 0.1	≤ 0.7	170 ± 0	−1.24
J0223.9–0353	02 23 59.44	0.5	−03 53 59.4	0.6	0.62	S	21.9 ± 2.0	≤ 3.3	≤ 2.7	134 ± 34	−1.00
J0223.9–0543	02 23 59.99	0.7	−05 43 58.1	1.3	1.24	S	16.5 ± 4.4	11.0 ± 3.4	≤ 5.4	15 ± 6	< −1.29
J0224.0–0325	02 24 00.56	0.7	−03 25 36.2	0.7	1.09	S	24.5 ± 4.1	8.2 ± 1.6	≤ 7.1	121 ± 11	< −1.56
J0224.0–0336	02 24 02.16	0.7	−03 36 05.1	0.9	0.91	S	8.7 ± 2.7	≤ 9.8	≤ 7.4	18 ± 36	< −0.86
J0224.0–0413	02 24 03.82	0.7	−04 13 38.8	0.8	0.31	S	5.7 ± 1.7	≤ 8.9	≤ 5.6	35 ± 23	< −0.57
J0224.0–0512	02 24 05.53	0.5	−05 12 29.6	0.6	0.72	S	16.0 ± 1.9	≤ 4.2	≤ 3.3	162 ± 30	−0.80
J0224.0–0520	02 24 05.64	0.7	−05 20 11.8	0.8	0.85	S	6.2 ± 1.9	≤ 6.9	≤ 5.8	NA	0.05
J0224.1–0450	02 24 10.21	0.5	−04 50 34.5	0.6	0.36	S	9.9 ± 1.5	≤ 3.8	≤ 3.8	NA	−0.40
J0224.1–0446	02 24 10.36	0.5	−04 46 09.1	0.6	0.30	M	104.1 ± 6.0	11.5			−1.14
	02 24 09.61	0.5	−04 46 07.0	0.6	0.30	C	32.7 ± 2.8	7.3 ± 0.7	3.9 ± 0.6	133 ± 5	−1.14
	02 24 10.36	0.5	−04 46 09.1	0.6	0.30	C	71.4 ± 4.0	4.5 ± 0.2	≤ 1.7	146 ± 2	−1.14
J0224.1–0350	02 24 10.82	0.5	−03 50 17.6	0.6	0.67	S	30.8 ± 2.4	3.4 ± 0.6	≤ 2.4	177 ± 8	−1.02
J0224.2–0355	02 24 12.15	0.6	−03 55 58.4	0.7	0.58	S	7.7 ± 1.8	≤ 7.1	≤ 4.8	103 ± 26	−0.24
J0224.2–0527*	02 24 12.70	0.5	−05 27 56.6	0.6	0.97	M	519.5 ± 26.7	58.5			−0.76
	02 24 12.70	0.5	−05 27 56.6	0.6	0.97	C	131.4 ± 7.0	4.9 ± 0.2	≤ 1.3	166 ± 1	−0.76

Table 2—Continued

Source	α (J2000) (h m s)	σ_α ($''$)	δ (J2000) ($^\circ$ ' $''$)	σ_δ ($''$)	Dist. ($^\circ$)	T.	S_{int} mJy	major ($''$)	Size minor ($''$)	PA ($^\circ$)	α
J0224.3–0502	02 24 14.96	0.5	−05 28 44.4	0.6	0.98	C	388.2 ± 20.2	20.8 ± 0.3	5.1 ± 0.1	150 ± 0	−0.76
	02 24 19.12	0.9	−05 02 37.9	0.6	0.55	S	22.7 ± 3.1	13.5 ± 1.9	≤ 3.6	92 ± 2	−1.08
	02 24 21.63	0.5	−04 25 50.2	0.6	0.10	M	124.5 ± 6.7	21.7			−1.21
J0224.3–0425	02 24 20.27	0.5	−04 25 42.8	0.6	0.11	C	51.3 ± 3.1	4.4 ± 0.3	2.2 ± 0.4	151 ± 4	−1.21
	02 24 21.63	0.5	−04 25 50.2	0.6	0.10	C	73.3 ± 4.0	3.9 ± 0.2	≤ 1.4	166 ± 2	−1.21
	02 24 27.58	1.0	−03 26 56.1	0.7	1.05	S	20.8 ± 4.2	11.0 ± 2.5	≤ 6.7	104 ± 6	−0.62
J0224.4–0326	02 24 28.73	0.6	−04 49 52.5	0.6	0.34	M	52.0 ± 5.1	19.4			−0.99
	02 24 27.44	0.9	−04 49 54.3	0.7	0.34	C	19.1 ± 3.4	10.6 ± 2.0	6.6 ± 1.5	88 ± 11	−0.99
	02 24 28.73	0.6	−04 49 52.5	0.6	0.34	C	32.9 ± 3.5	12.0 ± 1.2	4.5 ± 0.8	88 ± 3	−0.99
J0224.4–0504	02 24 29.28	0.5	−05 04 23.2	0.6	0.57	S	26.5 ± 2.1	≤ 3.5	≤ 2.8	151 ± 25	−1.13
J0224.4–0335	02 24 29.68	0.6	−03 35 29.8	0.8	0.91	S	8.1 ± 2.3	≤ 8.3	≤ 5.3	157 ± 23	−0.60
J0224.5–0534	02 24 32.15	0.5	−05 34 32.7	0.6	1.08	S	25.0 ± 2.6	≤ 4.4	≤ 3.0	179 ± 16	−0.22
J0224.5–0354	02 24 32.98	0.6	−03 54 38.9	0.7	0.59	S	12.9 ± 2.3	6.2 ± 1.6	≤ 5.0	155 ± 10	−0.55
J0224.5–0334	02 24 33.08	0.6	−03 34 11.9	0.7	0.93	S	53.0 ± 5.3	12.5 ± 1.2	6.2 ± 0.8	46 ± 4	−0.83
J0224.5–0408	02 24 33.86	0.5	−04 08 53.0	0.6	0.35	S	15.6 ± 1.8	≤ 4.6	≤ 3.1	169 ± 18	−1.06
J0224.5–0459	02 24 34.14	0.8	−04 59 01.0	0.8	0.48	S	7.9 ± 2.3	≤ 9.7	≤ 8.2	NA	−0.51
J0224.6–0347	02 24 39.74	0.5	−03 47 12.5	0.6	0.71	S	20.9 ± 2.6	5.7 ± 1.0	≤ 5.3	14 ± 12	−0.67
J0224.7–0330	02 24 44.35	0.5	−03 30 16.9	0.6	0.99	S	21.8 ± 2.6	4.2 ± 1.0	≤ 3.2	149 ± 10	−1.20
J0224.7–0351	02 24 44.83	0.7	−03 51 40.2	0.8	0.64	S	13.4 ± 2.7	≤ 9.2	≤ 8.4	NA	−0.76
J0224.7–0535	02 24 46.25	1.3	−05 35 51.8	0.8	1.10	S	13.4 ± 4.0	≤ 16.0	≤ 7.6	84 ± 10	< −1.15
J0224.7–0454	02 24 47.52	0.7	−04 54 34.5	0.9	0.41	S	6.1 ± 1.9	≤ 10.3	≤ 5.6	146 ± 17	< −0.61
J0224.8–0545	02 24 48.05	0.5	−05 45 22.8	0.6	1.26	M	204.7 ± 12.5	36.5			−1.03
	02 24 48.05	0.5	−05 45 22.8	0.6	1.26	C	112.5 ± 7.2	9.0 ± 0.4	3.9 ± 0.3	156 ± 2	−1.03
	02 24 49.72	0.5	−05 45 49.6	0.6	1.26	C	92.2 ± 7.2	11.1 ± 0.7	5.6 ± 0.5	127 ± 3	−1.03
J0224.8–0326	02 24 48.42	0.7	−03 26 11.5	0.8	1.06	S	6.6 ± 2.1	≤ 5.9	≤ 5.9	NA	< −0.66
J0224.8–0529	02 24 50.33	0.7	−05 29 24.8	0.7	0.99	S	6.4 ± 2.0	≤ 6.0	≤ 5.8	NA	< −0.64
J0224.8–0431	02 24 50.90	0.6	−04 31 41.1	0.7	0.05	S	4.9 ± 1.4	≤ 5.5	≤ 5.5	NA	< −0.46
J0224.8–0429	02 24 51.09	0.6	−04 29 01.8	0.8	0.05	S	9.0 ± 1.9	≤ 9.1	≤ 4.4	159 ± 10	< −0.88
J0224.8–0536	02 24 51.38	0.9	−05 36 59.2	0.8	1.12	M	18.8 ± 4.0	33.2			< −1.38
	02 24 50.44	0.7	−05 37 29.3	0.8	1.13	C	6.8 ± 2.3	≤ 6.0	≤ 6.0	NA	< −0.68
	02 24 51.38	0.9	−05 36 59.2	0.8	1.12	C	12.0 ± 3.3	≤ 12.3	≤ 5.5	114 ± 10	< −1.07
J0224.8–0434	02 24 53.87	0.5	−04 34 14.9	0.6	0.09	S	41.9 ± 2.7	5.0 ± 0.4	≤ 1.9	158 ± 3	−0.92
J0224.9–0332	02 24 54.87	0.5	−03 32 04.2	0.6	0.97	S	34.2 ± 2.8	4.0 ± 0.6	≤ 2.5	157 ± 6	−0.66
J0224.9–0329	02 24 54.93	0.5	−03 29 06.2	0.6	1.02	S	11.2 ± 2.1	≤ 4.4	≤ 4.3	NA	< −1.03
J0224.9–0310	02 24 55.70	0.5	−03 10 40.3	0.6	1.32	S	22.5 ± 3.3	≤ 5.7	≤ 3.6	142 ± 16	−0.67
J0224.9–0408	02 24 56.50	0.6	−04 08 54.9	0.7	0.36	S	6.7 ± 1.5	≤ 4.7	≤ 4.7	NA	< −0.67
J0224.9–0516	02 24 57.72	0.5	−05 16 48.8	0.6	0.78	M	160.7 ± 8.6	16.5			−1.00
	02 24 57.21	0.5	−05 17 03.5	0.6	0.79	C	79.8 ± 4.6	5.0 ± 0.2	2.5 ± 0.3	6 ± 3	−1.00
	02 24 57.72	0.5	−05 16 48.8	0.6	0.78	C	80.9 ± 4.5	4.5 ± 0.2	≤ 1.5	167 ± 2	−1.00
J0224.9–0435	02 24 59.45	0.7	−04 35 36.2	0.8	0.12	S	7.3 ± 1.9	≤ 10.1	≤ 5.0	145 ± 12	−0.68
J0225.0–0321	02 25 00.68	0.7	−03 21 07.8	0.8	1.15	M	54.1 ± 7.1	22.1			−0.95
	02 24 59.81	0.8	−03 20 50.0	1.1	1.16	C	22.8 ± 4.7	12.8 ± 2.9	≤ 5.8	144 ± 4	−0.95
	02 25 00.68	0.7	−03 21 07.8	0.8	1.15	C	31.4 ± 5.0	10.9 ± 1.8	4.9 ± 1.3	137 ± 6	−0.95
J0225.0–0536*	02 25 05.14	0.5	−05 36 48.5	0.6	1.12	S	837.0 ± 41.9	5.3 ± 0.0	≤ 0.6	166 ± 0	−0.86
J0225.0–0321	02 25 05.54	1.0	−03 21 18.7	0.9	1.15	S	10.6 ± 3.4	≤ 13.8	≤ 5.7	127 ± 10	< −0.99
J0225.0–0519	02 25 05.91	0.5	−05 19 59.8	0.6	0.84	S	16.7 ± 2.3	4.6 ± 1.2	≤ 3.5	164 ± 10	−0.54
J0225.1–0316	02 25 08.09	0.7	−03 16 37.0	1.8	1.23	S	48.5 ± 7.8	24.9 ± 4.2	5.2 ± 1.4	165 ± 2	−0.74
J0225.1–0401	02 25 09.19	0.5	−04 01 02.9	0.6	0.50	S	32.6 ± 2.3	3.0 ± 0.5	≤ 2.2	175 ± 8	−1.04
J0225.1–0404	02 25 10.24	0.5	−04 04 02.0	0.6	0.45	S	7.4 ± 1.5	≤ 4.6	≤ 4.6	NA	−0.47
J0225.1–0454	02 25 11.16	0.8	−04 54 32.8	0.8	0.43	M	59.2 ± 7.1	24.3			−0.75
	02 25 10.31	1.0	−04 54 34.8	0.9	0.43	C	24.4 ± 4.5	13.5 ± 2.6	9.4 ± 1.9	60 ± 15	−0.75
	02 25 11.16	0.8	−04 54 32.8	0.8	0.43	C	14.4 ± 3.0	7.6 ± 1.9	6.6 ± 1.8	NA	−0.75
J0225.2–0524	02 25 11.88	0.8	−04 54 28.4	0.9	0.43	C	20.4 ± 3.9	10.0 ± 2.1	9.3 ± 2.0	NA	−0.75
	02 25 12.13	0.5	−05 24 12.8	0.7	0.91	S	16.4 ± 2.8	6.7 ± 1.6	≤ 4.6	154 ± 8	−0.28
	02 25 12.96	0.6	−03 43 10.2	0.7	0.79	S	9.7 ± 2.2	≤ 8.1	≤ 4.7	160 ± 16	< −0.93
J0225.2–0436	02 25 14.91	0.5	−04 36 15.5	0.6	0.18	S	12.6 ± 1.7	≤ 6.0	≤ 3.5	168 ± 12	−0.75
J0225.2–0424	02 25 16.55	0.6	−04 24 26.6	0.7	0.18	S	7.2 ± 1.6	≤ 6.3	≤ 4.6	5 ± 32	< −0.73
J0225.3–0354	02 25 19.92	0.5	−03 54 41.0	0.6	0.61	S	28.1 ± 2.2	3.0 ± 0.6	≤ 2.4	179 ± 10	−1.09
J0225.4–0434	02 25 26.18	0.7	−04 34 56.0	0.8	0.21	S	4.1 ± 1.4	≤ 6.1	≤ 6.1	NA	< −0.34
J0225.4–0524	02 25 27.04	0.9	−05 24 57.3	0.9	0.94	S	12.3 ± 3.3	≤ 13.3	≤ 7.3	129 ± 13	< −1.09
J0225.4–0513	02 25 27.94	0.5	−05 13 44.6	0.8	0.76	S	10.8 ± 2.2	≤ 8.7	≤ 4.4	170 ± 11	< −1.00
J0225.4–0536	02 25 28.57	0.6	−05 36 57.2	0.7	1.13	S	8.9 ± 2.3	≤ 5.1	≤ 5.1	NA	−0.77
J0225.5–0439	02 25 30.33	0.7	−04 39 36.9	0.8	0.26	S	10.2 ± 2.4	≤ 9.7	≤ 8.4	NA	< −0.96
J0225.5–0502	02 25 35.07	0.8	−05 02 11.6	1.1	0.58	S	32.6 ± 5.2	15.5 ± 2.5	9.3 ± 1.6	16 ± 8	−0.82
J0225.6–0500	02 25 36.48	0.5	−05 00 12.3	0.6	0.56	S	40.9 ± 3.4	7.0 ± 0.6	5.1 ± 0.6	177 ± 9	−0.81
J0225.6–0406	02 25 37.62	0.5	−04 06 50.9	0.6	0.45	M	40.3 ± 3.3	31.1			−0.85

Table 2—Continued

Source	α (J2000) (h m s)	σ_α ($''$)	δ (J2000) ($^\circ$ ' $''$)	σ_δ ($''$)	Dist. ($^\circ$)	T.	S_{int} mJy	major ($''$)	Size minor ($''$)	PA ($^\circ$)	α
J0225.6–0417	02 25 37.62	0.5	−04 06 50.9	0.6	0.45	C	27.1 ± 2.3	4.5 ± 0.6	≤ 3.3	10 ± 7	−0.85
	02 25 39.17	0.5	−04 06 30.2	0.6	0.46	C	13.2 ± 2.0	4.8 ± 1.3	≤ 4.5	166 ± 14	−0.85
	02 25 40.12	0.6	−04 17 57.1	0.7	0.32	S	10.9 ± 2.2	≤ 7.8	≤ 7.2	NA	−0.61
	02 25 44.21	0.5	−03 16 33.3	0.7	1.25	S	14.6 ± 2.9	≤ 6.5	≤ 4.4	177 ± 23	−0.52
	02 25 45.58	1.3	−05 05 49.6	1.1	0.66	S	10.7 ± 3.0	12.6 ± 4.0	≤ 5.2	126 ± 5	< −1.00
J0225.7–0415	02 25 45.78	0.6	−04 15 29.2	0.7	0.36	S	9.8 ± 2.1	≤ 8.7	≤ 6.0	152 ± 20	−0.91
J0225.8–0400	02 25 49.76	0.6	−04 00 24.9	0.9	0.57	S	8.3 ± 2.1	≤ 10.5	≤ 5.2	179 ± 12	< −0.82
J0225.8–0422	02 25 50.23	0.5	−04 22 21.0	0.6	0.32	S	16.5 ± 1.8	≤ 5.1	≤ 3.0	163 ± 12	−0.79
J0225.8–0500	02 25 52.98	0.5	−05 00 17.3	0.6	0.59	M	19.8 ± 3.0	9.3			−0.66
	02 25 52.98	0.5	−05 00 17.3	0.6	0.59	C	9.1 ± 1.6	≤ 4.2	≤ 4.2	NA	−0.66
	02 25 53.53	0.7	−05 00 21.8	0.7	0.59	C	10.8 ± 2.4	≤ 9.8	≤ 6.9	105 ± 21	−0.66
J0225.9–0428	02 25 54.86	0.5	−04 28 55.0	0.6	0.31	M	35.6 ± 3.9	21.5			−0.95
	02 25 54.86	0.5	−04 28 55.0	0.6	0.31	C	21.1 ± 2.4	5.4 ± 0.9	4.5 ± 0.9	4 ± 27	−0.95
	02 25 56.24	0.8	−04 28 49.1	0.7	0.32	C	14.5 ± 2.8	9.0 ± 2.0	≤ 7.5	63 ± 10	−0.95
J0225.9–0545	02 25 55.40	0.5	−05 45 41.7	0.6	1.30	S	184.6 ± 10.2	8.1 ± 0.2	3.4 ± 0.2	28 ± 1	−0.78
J0225.9–0534	02 25 56.41	0.6	−05 34 51.3	0.7	1.13	S	9.3 ± 2.4	≤ 5.6	≤ 5.1	NA	0.10
J0225.9–0500	02 25 58.90	0.5	−05 00 54.7	0.6	0.61	S	11.9 ± 1.7	≤ 3.6	≤ 3.6	NA	−0.82
J0225.9–0444	02 25 58.95	0.8	−04 44 07.3	0.6	0.40	M	27.1 ± 3.7	12.4			−0.50
	02 25 58.95	0.8	−04 44 07.3	0.6	0.40	C	16.5 ± 2.9	10.3 ± 2.0	≤ 6.1	87 ± 6	−0.50
J0226.0–0429	02 25 59.78	0.7	−04 44 07.4	0.7	0.41	C	10.6 ± 2.1	6.5 ± 1.8	≤ 4.6	117 ± 9	−0.50
	02 26 03.11	0.6	−04 29 30.7	0.6	0.34	S	7.0 ± 1.5	≤ 4.6	≤ 4.6	NA	< −0.71
J0226.0–0431	02 26 03.58	0.5	−04 31 01.7	0.8	0.35	S	12.4 ± 2.3	8.3 ± 1.9	≤ 4.1	171 ± 5	0.18
J0226.0–0501	02 26 05.62	0.7	−05 01 10.7	0.8	0.63	S	5.0 ± 1.7	≤ 7.1	≤ 6.0	NA	< −0.48
J0226.1–0532	02 26 06.94	0.5	−05 32 17.9	0.6	1.10	S	54.4 ± 3.7	3.6 ± 0.4	≤ 2.1	172 ± 5	−0.15
J0226.1–0433	02 26 09.10	0.5	−04 33 36.5	0.6	0.38	S	40.9 ± 2.7	4.4 ± 0.4	≤ 2.0	173 ± 4	−1.14
J0226.1–0505	02 26 11.39	0.5	−05 05 07.5	0.6	0.70	S	12.3 ± 1.9	≤ 5.2	≤ 3.8	155 ± 26	< −1.09
J0226.2–0403	02 26 12.71	0.5	−04 03 19.9	0.6	0.59	S	11.2 ± 1.9	≤ 6.3	≤ 4.0	167 ± 17	−0.74
J0226.2–0422	02 26 15.29	0.5	−04 22 34.8	0.6	0.41	S	36.3 ± 2.5	3.6 ± 0.4	≤ 2.6	180 ± 7	−0.80
J0226.2–0504	02 26 17.45	0.5	−05 04 43.9	0.6	0.71	S	24.2 ± 2.2	3.4 ± 0.8	≤ 2.7	163 ± 10	−0.69
J0226.3–0400	02 26 18.80	0.5	−04 00 10.9	0.6	0.65	M	224.3 ± 16.1	53.3			−0.63
	02 26 17.23	0.9	−03 59 33.9	1.0	0.65	C	13.8 ± 3.5	8.4 ± 2.5	≤ 11.4	NA	−0.63
J0226.3–0425*	02 26 18.80	0.5	−04 00 10.9	0.6	0.65	C	115.1 ± 7.4	18.9 ± 0.8	6.6 ± 0.4	148 ± 1	−0.63
	02 26 19.06	1.6	−03 59 25.5	1.3	0.66	C	70.1 ± 10.3	26.6 ± 3.7	20.3 ± 2.9	87 ± 14	−0.63
	02 26 19.41	0.5	−04 00 16.1	0.6	0.65	C	25.4 ± 2.8	8.0 ± 1.0	≤ 3.5	158 ± 3	−0.63
	02 26 19.92	0.5	−04 25 39.8	0.6	0.42	M	172.9 ± 9.0	7.9			−1.01
	02 26 19.80	0.5	−04 25 32.2	0.6	0.42	C	85.8 ± 4.7	4.9 ± 0.2	2.2 ± 0.3	175 ± 2	−1.01
J0226.4–0333	02 26 19.92	0.5	−04 25 39.8	0.6	0.42	C	87.0 ± 4.7	5.0 ± 0.2	≤ 1.4	159 ± 1	−1.01
	02 26 27.19	0.6	−03 33 00.7	0.7	1.05	S	12.0 ± 2.7	≤ 8.3	≤ 4.6	139 ± 14	< −1.08
	02 26 32.55	0.5	−05 13 28.6	0.6	0.86	S	217.9 ± 11.1	4.0 ± 0.1	≤ 0.9	174 ± 1	−0.64
	02 26 34.16	0.5	−04 14 36.7	0.6	0.54	S	12.7 ± 1.8	≤ 5.6	≤ 3.6	165 ± 17	−0.60
	02 26 35.11	0.7	−04 11 26.8	0.8	0.57	S	4.6 ± 1.6	≤ 6.1	≤ 6.1	NA	< −0.41
J0226.6–0407	02 26 37.41	0.5	−04 07 59.7	0.6	0.61	S	15.5 ± 1.9	≤ 5.1	≤ 3.3	144 ± 16	−0.32
J0226.6–0501	02 26 38.96	0.8	−05 01 57.3	1.3	0.73	S	20.9 ± 4.3	14.5 ± 3.2	≤ 9.1	19 ± 6	−0.75
J0226.7–0446	02 26 42.28	0.6	−04 46 26.4	0.8	0.58	S	9.6 ± 2.1	≤ 9.8	≤ 4.6	157 ± 10	−0.37
J0226.7–0323	02 26 44.05	1.0	−03 23 55.1	1.0	1.22	S	15.1 ± 4.5	≤ 11.9	≤ 10.7	NA	−0.77
J0226.8–0359	02 26 52.26	0.6	−03 59 22.2	0.7	0.75	S	12.6 ± 2.5	≤ 8.3	≤ 6.7	21 ± 33	−0.82
J0226.9–0542	02 26 55.95	0.7	−05 42 42.8	0.7	1.34	S	32.2 ± 5.2	9.7 ± 1.8	≤ 5.8	65 ± 6	−1.67
J0226.9–0328	02 26 59.72	0.5	−03 28 20.9	0.6	1.18	M	72.2 ± 5.9	30.8			−0.89
	02 26 58.83	0.5	−03 28 48.7	0.6	1.17	C	34.0 ± 4.0	7.3 ± 1.0	≤ 4.5	16 ± 5	−0.89
	02 26 59.72	0.5	−03 28 20.9	0.6	1.18	C	38.2 ± 3.6	5.1 ± 0.7	≤ 3.3	9 ± 6	−0.89
J0227.0–0541	02 27 01.01	0.5	−05 41 50.5	0.6	1.33	S	46.4 ± 4.0	4.2 ± 0.6	≤ 2.5	165 ± 6	−0.84
J0227.1–0326	02 27 08.12	0.6	−03 26 01.2	0.7	1.23	M	190.8 ± 19.6	19.3			−1.11
	02 27 08.12	0.6	−03 26 01.2	0.7	1.23	C	43.5 ± 5.7	8.1 ± 1.2	7.6 ± 1.2	NA	−1.11
	02 27 09.09	0.8	−03 25 48.3	2.4	1.24	C	147.3 ± 17.9	49.3 ± 5.7	13.9 ± 1.6	5 ± 2	−1.11
J0227.2–0418	02 27 12.68	0.8	−04 18 19.7	0.7	0.66	S	7.8 ± 2.1	≤ 9.0	≤ 5.1	77 ± 16	< −0.78
J0227.2–0446	02 27 13.00	0.5	−04 46 36.7	0.6	0.69	S	17.9 ± 2.1	4.0 ± 1.0	≤ 3.2	179 ± 10	−0.42
J0227.2–0325	02 27 16.39	0.6	−03 25 37.3	0.6	1.25	M	63.1 ± 7.9	10.5			−0.28
	02 27 15.81	0.6	−03 25 43.2	2.0	1.25	C	32.4 ± 6.4	21.6 ± 4.6	≤ 5.8	174 ± 2	−0.28
J0227.2–0341	02 27 16.39	0.6	−03 25 37.3	0.6	1.25	C	30.7 ± 4.1	6.1 ± 1.1	≤ 5.9	114 ± 14	−0.28
	02 27 17.06	0.5	−03 41 08.7	0.6	1.04	S	49.3 ± 4.2	9.2 ± 0.8	≤ 3.5	99 ± 2	−0.77
J0227.3–0330	02 27 20.57	0.5	−03 30 37.8	0.6	1.19	S	22.9 ± 3.2	5.0 ± 1.2	≤ 3.5	156 ± 8	−1.46
J0227.3–0341	02 27 22.44	0.7	−03 41 22.5	0.7	1.05	S	8.4 ± 2.3	≤ 6.8	≤ 5.3	NA	−0.66
J0227.3–0433	02 27 22.82	0.6	−04 33 50.3	0.7	0.68	S	13.7 ± 2.5	5.8 ± 1.6	≤ 5.9	12 ± 17	< −1.16
J0227.4–0437	02 27 27.93	0.5	−04 37 35.0	0.6	0.71	S	92.1 ± 5.1	5.2 ± 0.2	≤ 1.4	171 ± 1	−0.98
J0227.4–0403	02 27 28.04	0.5	−04 03 39.7	0.6	0.82	M	32.3 ± 3.5	10.8			−1.28
	02 27 28.04	0.5	−04 03 39.7	0.6	0.82	C	20.3 ± 2.5	5.4 ± 1.0	≤ 3.2	157 ± 6	−1.28

Table 2—Continued

Source	α (J2000) (h m s)	σ_α ($''$)	δ (J2000) ($^\circ$ ' $''$)	σ_δ ($''$)	Dist. ($^\circ$)	T.	S_{int} mJy	major ($''$)	Size minor ($''$)	PA ($^\circ$)	α
J0227.5–0402	02 27 28.50	0.6	−04 03 48.0	0.7	0.82	C	12.0 \pm 2.2	≤ 5.9	≤ 5.6	NA	−1.28
	02 27 30.44	0.7	−04 02 18.7	0.9	0.84	S	7.1 \pm 2.3	≤ 10.0	≤ 5.8	163 \pm 19	−0.66
	02 27 30.52	0.5	−04 11 18.0	0.6	0.77	S	11.5 \pm 2.0	≤ 5.7	≤ 4.0	14 \pm 24	< −1.04
	02 27 31.26	0.6	−05 19 15.4	0.8	1.09	S	22.5 \pm 3.9	7.8 \pm 1.6	≤ 6.8	9 \pm 11	−0.76
	02 27 37.28	0.5	−04 11 07.9	0.6	0.80	M	83.4 \pm 8.4	57.0			−1.25
J0227.6–0411	02 27 34.22	0.8	−04 11 41.7	0.8	0.79	C	24.2 \pm 4.1	12.2 \pm 2.2	5.7 \pm 1.4	48 \pm 6	−1.25
	02 27 36.53	1.8	−04 11 08.1	1.2	0.80	C	32.8 \pm 5.8	26.1 \pm 4.8	5.6 \pm 1.5	121 \pm 2	−1.25
	02 27 37.28	0.5	−04 11 07.9	0.6	0.80	C	26.5 \pm 2.9	5.8 \pm 0.9	3.5 \pm 0.9	148 \pm 10	−1.25
	02 27 39.14	1.2	−03 24 04.1	1.0	1.33	S	16.8 \pm 4.8	11.5 \pm 3.8	≤ 5.3	125 \pm 6	< −1.30
	02 27 42.97	0.7	−03 40 13.6	0.8	1.12	S	6.8 \pm 2.3	≤ 6.2	≤ 6.0	NA	< −0.69
J0227.7–0502	02 27 43.69	0.5	−05 02 52.3	0.6	0.94	S	37.9 \pm 3.2	6.7 \pm 0.7	≤ 2.5	159 \pm 3	−0.75
J0227.8–0429	02 27 52.80	0.5	−04 29 42.6	0.6	0.80	S	10.1 \pm 1.8	≤ 4.2	≤ 4.2	NA	< −0.96
J0227.8–0343	02 27 53.47	0.5	−03 43 54.3	0.6	1.11	S	28.9 \pm 3.5	5.1 \pm 1.0	4.3 \pm 1.0	40 \pm 36	−0.76
J0227.8–0444	02 27 53.94	0.5	−04 44 52.1	0.6	0.84	M	56.5 \pm 5.0	10.5			−1.04
J0227.9–0457	02 27 53.94	0.5	−04 44 52.1	0.6	0.84	C	37.6 \pm 3.4	8.5 \pm 0.8	≤ 3.8	169 \pm 3	−1.04
	02 27 54.49	0.5	−04 44 58.5	0.9	0.84	C	18.9 \pm 3.1	9.9 \pm 1.8	≤ 3.8	173 \pm 4	−1.04
	02 27 54.87	0.5	−04 57 04.9	0.6	0.93	S	84.6 \pm 4.8	3.9 \pm 0.2	≤ 1.5	171 \pm 2	−0.49
	02 27 59.95	0.8	−04 00 15.4	1.2	0.97	S	19.4 \pm 4.6	12.1 \pm 3.1	≤ 9.5	20 \pm 10	−0.97
	02 28 03.39	0.9	−04 14 13.3	1.3	0.89	M	39.0 \pm 6.9	13.0			−1.69
J0228.0–0414	02 28 02.57	1.2	−04 14 17.5	1.0	0.88	C	16.9 \pm 4.5	10.5 \pm 3.1	≤ 11.9	104 \pm 24	−1.69
	02 28 03.39	0.9	−04 14 13.3	1.3	0.89	C	22.0 \pm 5.1	13.8 \pm 3.3	7.5 \pm 2.2	158 \pm 11	−1.69
	02 28 05.52	0.5	−05 05 49.1	0.6	1.04	S	14.2 \pm 2.3	≤ 4.7	≤ 3.9	NA	< −1.19
	02 28 08.53	0.5	−04 08 51.4	0.6	0.94	S	17.4 \pm 2.6	≤ 6.4	≤ 4.8	159 \pm 21	−0.78
	02 28 14.44	0.5	−05 02 41.3	0.8	1.04	S	46.7 \pm 5.6	12.0 \pm 1.4	7.0 \pm 1.0	177 \pm 6	−0.37
J0228.3–0405	02 28 19.15	0.7	−04 05 00.7	0.8	1.00	S	13.9 \pm 3.3	≤ 9.8	≤ 8.0	47 \pm 38	< −1.17
J0228.3–0432	02 28 20.81	0.6	−04 32 27.6	0.8	0.92	S	12.6 \pm 2.8	≤ 8.5	≤ 7.0	162 \pm 40	< −1.11
J0228.3–0430	02 28 23.31	0.5	−04 30 26.0	0.6	0.93	M	60.3 \pm 5.1	18.5			−0.97
J0228.4–0427	02 28 22.95	0.7	−04 30 08.2	0.7	0.93	C	11.0 \pm 2.5	≤ 9.2	≤ 4.7	111 \pm 12	−0.97
	02 28 23.31	0.5	−04 30 26.0	0.6	0.93	C	49.2 \pm 4.1	10.4 \pm 0.8	≤ 3.2	144 \pm 2	−0.97
	02 28 24.08	1.0	−04 27 09.1	0.9	0.93	S	17.2 \pm 4.0	10.3 \pm 2.7	≤ 8.6	122 \pm 11	−0.37
	02 28 25.38	0.5	−04 34 40.9	0.6	0.94	S	17.1 \pm 2.4	≤ 5.8	≤ 3.5	167 \pm 14	−0.65
	02 28 26.87	0.6	−04 17 52.0	0.8	0.96	S	10.3 \pm 2.5	≤ 9.3	≤ 4.9	154 \pm 14	< −0.97
J0228.5–0446	02 28 31.67	0.5	−04 46 05.4	0.6	1.00	S	28.9 \pm 3.0	6.1 \pm 0.8	≤ 2.9	152 \pm 4	−0.91
J0228.5–0347	02 28 33.69	0.7	−03 47 37.4	1.0	1.20	S	9.9 \pm 3.2	≤ 11.5	≤ 5.8	160 \pm 14	< −0.95
J0228.5–0340	02 28 34.66	0.5	−03 40 00.9	0.6	1.28	S	27.2 \pm 2.9	≤ 3.0	≤ 3.0	NA	−0.58
J0228.6–0449	02 28 36.57	0.7	−04 49 30.2	1.0	1.03	S	16.7 \pm 4.0	8.4 \pm 2.4	≤ 9.0	2 \pm 20	< −1.30
J0228.6–0406	02 28 38.56	0.5	−04 06 48.5	0.6	1.06	M	55.2 \pm 5.4	59.5			−0.62
J0228.6–0435	02 28 34.68	0.7	−04 06 35.4	1.3	1.05	C	13.6 \pm 4.0	≤ 16.5	≤ 7.9	175 \pm 10	−0.62
	02 28 38.56	0.5	−04 06 48.5	0.6	1.06	C	41.5 \pm 3.3	4.6 \pm 0.6	≤ 2.4	163 \pm 4	−0.62
	02 28 39.38	0.5	−04 35 53.6	0.6	1.00	M	38.7 \pm 3.8	12.4			−0.87
	02 28 39.38	0.5	−04 35 53.6	0.6	1.00	C	19.6 \pm 2.5	≤ 5.6	≤ 3.3	171 \pm 13	−0.87
	02 28 39.84	0.5	−04 35 43.4	0.6	1.00	C	19.1 \pm 2.5	≤ 6.0	≤ 3.4	9 \pm 11	−0.87
J0228.7–0350	02 28 42.38	0.6	−03 50 19.5	0.9	1.21	S	10.8 \pm 3.2	≤ 10.5	≤ 5.4	5 \pm 14	< −1.00
J0228.7–0502	02 28 45.63	0.6	−05 02 31.6	0.7	1.16	S	16.2 \pm 3.3	≤ 8.6	≤ 5.9	154 \pm 19	−1.05
J0228.8–0350	02 28 53.60	0.5	−03 50 55.8	0.6	1.24	S	30.3 \pm 3.3	3.6 \pm 0.9	≤ 4.0	13 \pm 22	−0.65
J0228.9–0504	02 28 57.44	0.6	−05 04 51.3	1.0	1.22	S	14.5 \pm 3.7	≤ 12.8	≤ 4.9	159 \pm 8	−0.90
J0229.0–0445	02 29 00.56	0.7	−04 45 43.9	0.8	1.11	S	6.4 \pm 2.2	≤ 6.1	≤ 6.1	NA	< −0.65
J0229.0–0421	02 29 05.04	0.5	−04 21 22.2	0.6	1.11	S	26.5 \pm 2.9	4.2 \pm 0.9	≤ 3.0	173 \pm 8	−0.69
J0229.0–0402	02 29 05.98	0.5	−04 02 42.3	0.6	1.20	S	66.6 \pm 4.9	6.2 \pm 0.5	3.7 \pm 0.5	30 \pm 5	−0.43
J0229.1–0508	02 29 08.59	0.5	−05 08 31.8	0.7	1.29	S	13.4 \pm 2.8	≤ 5.1	≤ 4.5	NA	−0.76
J0229.1–0507	02 29 08.76	0.5	−05 07 25.7	0.6	1.28	S	49.4 \pm 4.4	5.9 \pm 0.7	≤ 3.7	170 \pm 5	−1.10
J0229.1–0406	02 29 10.79	0.5	−04 06 07.3	0.8	1.19	S	33.6 \pm 4.5	12.0 \pm 1.7	≤ 3.4	161 \pm 2	−1.25
J0229.2–0359	02 29 12.77	0.8	−03 59 37.1	1.2	1.24	S	12.4 \pm 3.9	≤ 14.9	≤ 5.6	153 \pm 9	< −1.09
J0229.2–0511	02 29 13.03	0.7	−05 11 20.3	0.8	1.33	S	8.4 \pm 2.8	≤ 5.9	≤ 5.9	NA	−0.40
J0229.2–0442*	02 29 15.76	0.5	−04 42 17.1	0.6	1.16	M	1280.8 \pm 64.3	8.3			−0.88
J0229.2–0403	02 29 15.76	0.5	−04 42 17.1	0.6	1.16	C	892.0 \pm 44.7	5.9 \pm 0.0	≤ 0.6	166 \pm 0	−0.88
	02 29 16.19	0.5	−04 42 11.8	0.6	1.17	C	388.8 \pm 19.9	7.3 \pm 0.1	6.5 \pm 0.1	98 \pm 4	−0.88
	02 29 17.27	0.5	−04 03 28.1	0.6	1.23	S	27.0 \pm 3.2	4.4 \pm 1.0	≤ 3.2	146 \pm 9	−0.56
	02 29 18.73	0.9	−05 05 13.1	1.0	1.30	S	19.8 \pm 4.9	11.0 \pm 3.1	≤ 5.9	137 \pm 6	−0.92
	02 29 19.22	0.7	−04 29 46.8	1.2	1.16	S	11.4 \pm 3.5	≤ 14.4	≤ 5.6	10 \pm 9	< −1.04
J0229.3–0429	02 29 22.09	0.5	−04 54 27.4	0.7	1.24	S	43.1 \pm 4.5	9.7 \pm 1.1	≤ 2.9	180 \pm 2	−0.97
J0229.3–0454	02 29 22.45	0.5	−04 07 29.5	0.6	1.23	S	20.3 \pm 2.8	≤ 4.6	≤ 3.6	14 \pm 31	−0.90
J0229.3–0407	02 29 25.33	0.9	−04 19 02.2	1.4	1.20	S	15.7 \pm 4.4	12.5 \pm 4.0	≤ 5.2	150 \pm 5	< −1.26
J0229.4–0419	02 29 27.75	0.6	−04 38 39.5	0.9	1.20	S	10.9 \pm 3.1	≤ 10.0	≤ 5.4	12 \pm 15	< −1.01
J0229.4–0438	02 29 33.15	0.8	−04 02 39.1	1.4	1.30	S	16.2 \pm 4.7	11.6 \pm 3.8	≤ 5.3	158 \pm 6	< −1.28
J0229.5–0402	02 29 36.56	0.6	−04 35 17.5	0.7	1.24	S	11.0 \pm 2.8	≤ 6.8	≤ 5.1	151 \pm 36	−0.80

Table 2—Continued

Source	α (J2000) (h m s)	σ_α ($''$)	δ (J2000) ($^\circ$ ' $''$)	σ_δ ($''$)	Dist. ($^\circ$)	T.	S_{int} mJy	major ($''$)	Size minor ($''$)	PA ($^\circ$)	α
J0229.6–0442	02 29 38.00	0.6	–04 42 42.4	0.7	1.26	S	11.4 ± 2.6	≤ 4.8	≤ 4.8	NA	–0.41
J0229.8–0447	02 29 51.33	0.6	–04 47 39.7	0.7	1.33	M	31.1 ± 5.8	7.4			–0.78
	02 29 50.96	0.6	–04 47 44.6	1.4	1.32	C	15.9 ± 4.6	≤ 17.1	≤ 5.3	177 ± 6	–0.78
	02 29 51.33	0.6	–04 47 39.7	0.7	1.33	C	15.3 ± 3.3	≤ 7.5	≤ 4.6	168 ± 18	–0.78

Note. — An asterisk (*) after the sourcename indicates this source was also detected at 74 MHz.

Note. — Positions of multiple sources are given as the position of the peak component.

Note. — Description of columns:

1. Source Name
2. Right Ascension (J2000)
3. Right Ascension uncertainty in arcseconds
4. Declination (J2000)
5. Declination uncertainty in arcseconds
6. Distance from pointing center in degrees
7. Source type: Single (S), Multiple (M) or Component (C) of multiple source
8. Integrated Flux in mJy
9. Size of Major Axis in arcseconds, or the 2σ upper limit if the source is unresolved
10. Size of Minor Axis in arcseconds, or the 2σ upper limit if the source is unresolved
11. PA of Major axis in degrees.
12. Spectral index with respect to NVSS flux (1.4 GHz).

Table 3. 74 MHz Source List

Source	α (J2000) (h m s)	σ_α ($''$)	δ (J2000) ($^\circ$ ' $''$)	σ_δ ($''$)	Dist. ($^\circ$)	T.	S_{int} Jy	major ($''$)	Size minor ($''$)	PA ($^\circ$)	α
J0201.7–0419	02 01 45.21	5.5	–04 19 24.8	3.6	5.71	S	0.95 ± 0.29	≤ 76.2	≤ 26.2	62 ± 7	–0.66
J0202.9–0605	02 02 56.33	3.2	–06 05 22.5	2.2	5.64	S	2.22 ± 0.33	44.5 ± 11.6	≤ 24.1	66 ± 4	–0.66
J0204.9–0655	02 04 54.31	3.7	–06 55 10.5	3.5	5.48	S	2.00 ± 0.37	50.6 ± 14.3	≤ 37.0	46 ± 7	–0.44
J0204.9–0715	02 04 54.90	6.8	–07 15 56.4	3.1	5.64	S	1.87 ± 0.42	67.8 ± 19.8	≤ 38.4	78 ± 5	–0.67
J0206.0–0511	02 06 03.21	2.3	–05 11 30.5	2.3	4.69	M	3.38 ± 0.41	44.4			–0.74
	02 06 03.21	2.3	–05 11 30.5	2.3	4.69	C	1.61 ± 0.23	≤ 47.3	≤ 21.9	36 ± 6	–0.74
	02 06 06.11	4.0	–05 11 40.3	3.2	4.68	C	1.77 ± 0.32	54.8 ± 14.2	≤ 33.7	55 ± 5	–0.74
J0206.0–0503	02 06 04.29	3.0	–05 03 35.9	2.2	4.67	S	2.40 ± 0.33	45.4 ± 10.6	≤ 37.3	73 ± 7	–0.59
J0206.2–0553	02 06 16.43	3.1	–05 53 26.2	2.2	4.79	S	1.29 ± 0.24	≤ 50.9	≤ 26.8	71 ± 9	–0.39
J0207.9–0527	02 07 57.08	2.2	–05 27 20.3	1.7	4.27	S	2.26 ± 0.22	32.0 ± 9.0	≤ 13.3	69 ± 3	–0.60
J0208.3–0708	02 08 19.65	4.8	–07 08 22.5	3.9	4.84	S	1.12 ± 0.30	≤ 70.3	≤ 45.4	60 ± 17	–0.74
J0208.4–0047	02 08 25.96	2.1	–00 47 44.0	1.9	5.49	S	1.41 ± 0.21	≤ 24.6	≤ 23.0	NA	–0.30
J0209.1–0308	02 09 06.84	2.9	–03 08 06.7	2.4	4.11	S	0.98 ± 0.19	≤ 48.1	≤ 22.6	56 ± 8	–0.51
J0209.5–0736	02 09 31.29	2.2	–07 36 48.6	2.1	4.88	S	3.32 ± 0.34	39.6 ± 8.4	≤ 34.1	39 ± 6	–0.75
J0209.6–0059	02 09 37.81	4.8	–00 59 55.9	4.1	5.13	S	1.08 ± 0.31	≤ 66.7	≤ 48.5	60 ± 26	–0.61
J0209.7–0137	02 09 45.07	1.9	–01 37 35.2	1.7	4.70	S	3.17 ± 0.26	24.4 ± 9.2	≤ 19.3	45 ± 4	–0.45
J0209.7–0512	02 09 45.13	3.7	–05 12 11.7	2.7	3.78	S	0.83 ± 0.20	≤ 55.1	≤ 29.5	64 ± 11	–0.72
J0210.2–0344	02 10 15.80	3.4	–03 44 09.8	1.8	3.67	M	4.83 ± 0.43	48.6			–0.82
	02 10 12.57	2.6	–03 44 05.3	1.8	3.69	C	1.12 ± 0.17	≤ 42.5	≤ 17.8	82 ± 6	–0.82
	02 10 15.80	3.4	–03 44 09.8	1.8	3.67	C	3.71 ± 0.37	77.1 ± 9.2	≤ 33.9	89 ± 2	–0.82
J0210.6–0014	02 10 40.27	4.1	–00 14 32.8	3.8	5.51	S	1.30 ± 0.34	≤ 61.3	≤ 46.6	52 ± 28	–0.77
J0210.8–0633	02 10 53.06	7.0	–06 33 38.3	2.6	4.00	S	2.62 ± 0.40	105.5 ± 18.3	≤ 37.3	80 ± 2	–0.47
J0211.0–0644	02 11 05.16	1.9	–06 44 44.3	1.6	4.06	S	3.99 ± 0.29	26.5 ± 8.0	≤ 27.5	70 ± 7	–0.61
J0212.0–0307	02 12 05.51	1.9	–03 07 23.8	1.7	3.43	S	2.11 ± 0.18	≤ 30.4	≤ 14.2	38 ± 5	–0.80
J0212.5–0820	02 12 34.45	3.7	–08 20 36.7	3.4	4.88	M	2.77 ± 0.43	48.7			–0.59
	02 12 34.45	3.7	–08 20 36.7	3.4	4.88	C	1.46 ± 0.31	≤ 67.8	≤ 38.8	48 ± 10	–0.59
	02 12 34.76	3.8	–08 21 25.2	4.1	4.89	C	1.31 ± 0.28	50.1 ± 16.8	≤ 27.7	40 ± 5	–0.59
J0213.1–0141	02 13 11.14	3.5	–01 41 06.4	2.7	4.02	S	1.68 ± 0.28	45.6 ± 12.7	≤ 38.6	116 ± 8	–0.80
J0213.1–0457	02 13 11.99	2.0	–04 57 21.0	1.7	2.89	S	2.13 ± 0.19	24.0 ± 9.8	≤ 19.6	50 ± 5	–0.61
J0213.2–0719	02 13 16.62	3.2	–07 19 34.7	3.4	4.00	S	0.96 ± 0.20	≤ 64.0	≤ 21.2	39 ± 5	–0.35
J0213.3–0435	02 13 23.36	2.7	–04 35 00.4	2.1	2.81	S	1.08 ± 0.17	≤ 47.6	≤ 21.0	62 ± 6	–0.94
J0213.4–0420	02 13 24.71	2.4	–04 20 01.2	1.7	2.81	S	3.05 ± 0.28	48.7 ± 7.4	≤ 29.9	85 ± 3	–1.04
J0213.7–0256	02 13 46.80	2.0	–02 56 39.8	2.4	3.13	S	2.44 ± 0.25	46.8 ± 8.3	≤ 24.5	11 ± 3	–0.67
J0214.2–0153	02 14 16.68	3.8	–01 53 13.9	2.7	3.68	S	0.85 ± 0.20	≤ 52.7	≤ 35.9	87 ± 19	–0.57
J0214.4–0720	02 14 27.05	3.3	–07 20 11.5	2.7	3.81	S	1.44 ± 0.25	41.2 ± 13.1	≤ 35.1	59 ± 8	–0.89
J0214.6–0603	02 14 36.10	2.8	–06 03 46.5	2.2	2.95	S	1.09 ± 0.17	≤ 52.1	≤ 18.1	59 ± 5	–0.76
J0214.9–0453	02 14 60.00	2.7	–04 53 49.4	3.6	2.44	S	1.29 ± 0.23	43.0 ± 13.3	≤ 41.1	5 ± 11	–0.77
J0215.0–0600	02 15 05.31	2.5	–06 00 52.1	1.9	2.83	S	1.07 ± 0.16	≤ 42.7	≤ 17.2	67 ± 6	–0.80
J0215.1–0702	02 15 07.65	2.2	–07 02 06.4	1.9	3.47	S	2.06 ± 0.21	36.2 ± 8.8	≤ 17.8	52 ± 3	–0.67
J0215.1–0135	02 15 10.10	2.1	–01 35 25.8	1.8	3.75	S	1.52 ± 0.18	≤ 34.5	≤ 19.6	60 ± 8	–1.00
J0215.1–0343	02 15 11.43	2.4	–03 43 09.1	2.1	2.49	S	0.77 ± 0.14	≤ 36.2	≤ 19.4	51 ± 11	–0.48
J0215.2–0153	02 15 17.15	2.4	–01 53 28.6	2.1	3.50	S	0.63 ± 0.13	≤ 26.7	≤ 21.9	NA	–0.75
J0215.3+0040	02 15 19.20	2.7	+00 40 49.8	3.0	5.68	S	1.09 ± 0.25	≤ 45.8	≤ 26.8	152 ± 14	–0.56
J0215.5–0321	02 15 34.37	3.9	–03 21 59.9	3.9	2.54	S	0.70 ± 0.18	≤ 66.0	≤ 32.0	43 ± 10	–0.63
J0215.5–0710	02 15 34.75	3.2	–07 10 58.5	2.9	3.51	S	0.60 ± 0.16	≤ 39.5	≤ 34.9	NA	–0.53
J0215.6–0206	02 15 37.54	3.5	–02 06 07.6	2.8	3.29	S	0.62 ± 0.16	≤ 46.9	≤ 30.0	67 ± 19	–0.93
J0215.6–0056	02 15 39.90	5.6	–00 56 59.8	3.2	4.20	S	0.74 ± 0.22	≤ 74.6	≤ 28.8	70 ± 8	–1.03
J0215.6–0222	02 15 41.98	1.8	–02 22 52.0	1.5	3.08	S	4.42 ± 0.27	≤ 23.4	≤ 19.7	26 ± 11	–0.75
J0215.7–0142	02 15 45.23	2.1	–01 42 50.2	1.9	3.56	S	0.86 ± 0.13	≤ 22.4	≤ 18.2	48 ± 42	–0.64
J0215.9–0344	02 15 59.70	2.5	–03 44 19.6	1.9	2.29	S	0.96 ± 0.14	≤ 39.3	≤ 17.5	74 ± 7	–0.72
J0216.2+0009	02 16 16.69	2.5	+00 09 01.3	2.4	5.10	S	0.64 ± 0.16	≤ 24.4	≤ 24.1	NA	–0.42
J0216.6–0613	02 16 41.86	4.1	–06 13 51.6	3.7	2.63	S	0.54 ± 0.16	≤ 62.4	≤ 25.8	50 ± 10	–0.84
J0217.0–0954	02 17 01.71	3.0	–09 54 45.0	3.4	5.73	S	0.98 ± 0.25	≤ 50.6	≤ 26.4	30 ± 13	–0.73
J0217.0–0603	02 17 02.28	2.7	–06 03 29.7	2.0	2.46	S	0.80 ± 0.14	≤ 39.9	≤ 19.3	73 ± 9	–1.49
J0217.0–0210	02 17 02.96	2.9	–02 10 43.4	2.3	3.00	S	0.63 ± 0.14	≤ 38.6	≤ 22.2	113 ± 15	–0.63
J0217.4–0052	02 17 28.57	2.0	–00 52 27.8	1.8	4.05	S	0.97 ± 0.14	≤ 17.4	≤ 17.2	NA	–0.51
J0217.5–0046	02 17 32.32	2.8	–00 46 59.6	2.6	4.12	S	0.67 ± 0.16	≤ 38.3	≤ 23.3	47 ± 18	–0.63
J0217.7–0030	02 17 46.43	1.9	–00 30 24.3	1.8	4.35	M	2.56 ± 0.24	44.4			–0.72
	02 17 44.88	2.1	–00 29 46.6	1.9	4.36	C	0.85 ± 0.14	≤ 19.2	≤ 19.0	NA	–0.72
	02 17 46.43	1.9	–00 30 24.3	1.8	4.35	C	1.71 ± 0.18	≤ 27.1	≤ 14.1	174 ± 8	–0.72
J0218.1–0301	02 18 11.78	4.1	–03 01 26.1	2.8	2.19	S	0.51 ± 0.15	≤ 53.0	≤ 27.7	110 ± 14	–0.94
J0218.4–0454	02 18 27.30	2.1	–04 54 39.6	1.9	1.60	S	0.97 ± 0.13	≤ 33.0	≤ 16.4	51 ± 8	–0.84
J0218.6–0725	02 18 37.73	2.5	–07 25 31.6	2.2	3.29	S	1.17 ± 0.18	≤ 45.5	≤ 23.8	49 ± 8	–0.72
J0218.6–0441	02 18 39.39	2.8	–04 41 48.8	2.4	1.51	S	0.95 ± 0.16	≤ 52.0	≤ 23.2	51 ± 6	–0.97
J0218.8–0211	02 18 50.79	1.9	–02 11 14.9	1.6	2.73	S	1.76 ± 0.16	≤ 24.2	≤ 18.5	66 ± 16	–0.67
J0218.9–0149	02 18 57.11	2.5	–01 49 11.1	1.9	3.04	S	0.90 ± 0.15	≤ 36.7	≤ 18.6	78 ± 10	–0.56

Table 3—Continued

Source	α (J2000) (h m s)	σ_α ($''$)	δ (J2000) ($^\circ$ ' $''$)	σ_δ ($''$)	Dist. ($^\circ$)	T.	S_{int} Jy	major ($''$)	Size minor ($''$)	PA ($^\circ$)	α
J0218.9–0155	02 18 57.63	2.2	−01 55 33.0	2.0	2.94	S	0.68 ± 0.12	≤ 22.9	≤ 19.6	NA	−0.81
J0219.1–0252	02 19 07.30	2.0	−02 52 49.7	1.8	2.13	S	0.74 ± 0.11	≤ 17.8	≤ 17.8	NA	−0.37
J0219.4–0539	02 19 28.19	1.8	−05 39 47.8	1.5	1.74	S	4.16 ± 0.25	18.1 ± 9.5	≤ 17.6	44 ± 3	−0.81
J0219.4–0251	02 19 29.85	2.1	−02 51 11.9	1.7	2.09	S	1.03 ± 0.13	≤ 25.6	≤ 15.7	97 ± 13	−0.75
J0219.5–0058	02 19 32.26	2.8	−00 58 28.3	2.3	3.75	S	0.85 ± 0.17	≤ 42.4	≤ 20.4	122 ± 10	−0.78
J0220.5+0027	02 20 33.43	3.6	+00 27 57.7	3.4	5.07	S	0.59 ± 0.20	≤ 40.6	≤ 36.1	NA	−0.55
J0220.9–0725	02 20 54.22	3.4	−07 25 47.8	2.7	3.08	S	0.51 ± 0.14	≤ 44.4	≤ 25.3	62 ± 17	−0.57
J0220.9–0156	02 20 54.26	1.8	−01 56 52.5	1.5	2.72	S	34.89 ± 1.75	≤ 17.9	≤ 11.5	18 ± 1	−0.79
J0220.9–0348*	02 20 55.69	1.9	−03 48 34.2	1.7	1.16	S	1.45 ± 0.14	≤ 26.5	≤ 15.5	54 ± 8	−0.98
J0221.0+0059	02 21 03.68	1.9	+00 59 38.7	1.8	5.57	S	1.71 ± 0.21	≤ 23.0	≤ 15.5	178 ± 18	−0.58
J0221.1–0931	02 21 07.01	4.0	−09 31 44.4	4.0	5.11	S	0.89 ± 0.24	≤ 67.5	≤ 24.7	44 ± 8	−0.86
J0221.2–0255	02 21 16.37	2.4	−02 55 49.9	2.2	1.78	S	0.44 ± 0.10	≤ 23.1	≤ 23.1	NA	−0.52
J0221.7–0451*	02 21 42.09	2.2	−04 51 10.6	2.1	0.82	S	0.56 ± 0.10	≤ 22.7	≤ 20.2	NA	−0.79
J0221.7–0413*	02 21 43.02	1.8	−04 13 42.8	1.5	0.78	S	2.47 ± 0.16	≤ 16.5	≤ 10.2	16 ± 9	−0.53
J0222.0–0240	02 22 00.91	2.5	−02 40 05.6	2.0	1.95	S	0.99 ± 0.15	≤ 43.1	≤ 17.3	118 ± 6	−0.63
J0222.2–0009	02 22 17.93	2.2	−00 09 28.9	2.0	4.38	S	0.77 ± 0.14	≤ 21.9	≤ 20.4	NA	−0.78
J0222.3–0242	02 22 20.70	2.0	−02 42 18.8	1.8	1.89	S	0.96 ± 0.12	≤ 24.0	≤ 16.0	35 ± 17	−1.09
J0222.6+0059	02 22 39.36	2.5	+00 59 23.7	2.5	5.51	S	0.88 ± 0.20	≤ 34.2	≤ 22.8	31 ± 23	−0.62
J0222.9–0518*	02 22 55.78	1.9	−05 18 18.2	1.7	0.91	S	1.83 ± 0.15	≤ 28.6	≤ 17.4	31 ± 7	−0.66
J0222.9–0602	02 22 55.86	3.4	−06 02 06.8	4.5	1.59	S	0.52 ± 0.16	≤ 60.2	≤ 35.3	21 ± 17	−0.85
J0222.9–0243	02 22 56.13	1.8	−02 43 03.4	1.6	1.83	M	3.98 ± 0.25	≤ 37.0			−0.76
	02 22 56.13	1.8	−02 43 03.4	1.6	1.83	C	2.41 ± 0.16	≤ 14.5	≤ 12.7	162 ± 36	−0.76
	02 22 58.50	1.8	−02 42 53.0	1.6	1.83	C	1.57 ± 0.13	≤ 18.4	≤ 12.2	10 ± 14	−0.76
J0222.9–0630	02 22 57.90	2.7	−06 30 59.2	2.6	2.06	S	0.47 ± 0.12	≤ 34.9	≤ 23.9	37 ± 27	−0.62
J0223.0–0826	02 23 01.54	4.0	−08 26 13.0	3.3	3.96	S	0.52 ± 0.17	≤ 52.8	≤ 27.4	55 ± 15	−0.46
J0223.0–0107	02 23 03.32	2.8	−01 07 44.8	2.7	3.40	S	0.52 ± 0.14	≤ 35.4	≤ 24.5	40 ± 28	−1.01
J0223.1–0750	02 23 11.22	2.2	−07 50 35.1	2.0	3.36	S	1.05 ± 0.16	≤ 30.8	≤ 23.1	50 ± 21	−0.60
J0223.5–0713	02 23 32.90	3.7	−07 13 58.0	3.7	2.75	S	0.91 ± 0.21	≤ 68.1	≤ 34.4	43 ± 9	−0.69
J0223.5–0301	02 23 33.30	2.9	−03 01 22.2	2.7	1.50	S	0.75 ± 0.15	≤ 47.2	≤ 29.2	46 ± 14	−0.99
J0223.5–0232	02 23 34.82	2.3	−02 32 16.5	2.1	1.98	S	0.49 ± 0.10	≤ 22.0	≤ 22.0	NA	−0.80
J0223.5–0637	02 23 35.04	2.4	−06 37 25.5	2.3	2.14	S	1.08 ± 0.17	≤ 42.2	≤ 29.0	35 ± 14	−0.97
J0223.6–0213	02 23 38.12	2.8	−02 13 51.8	2.7	2.28	S	0.35 ± 0.11	≤ 26.9	≤ 26.9	NA	−1.01
J0223.6–0239	02 23 41.76	2.2	−02 39 41.0	2.0	1.85	S	0.60 ± 0.11	≤ 21.4	≤ 19.9	NA	−0.85
J0223.9–0441*	02 23 57.04	2.0	−04 41 11.0	1.8	0.26	S	0.78 ± 0.11	≤ 20.8	≤ 16.9	27 ± 40	−0.91
J0224.0–0638	02 24 00.69	1.9	−06 38 44.8	1.7	2.15	S	1.52 ± 0.14	≤ 25.6	≤ 13.0	34 ± 7	−0.85
J0224.0–0103	02 24 04.79	2.7	−01 03 44.7	2.5	3.44	S	0.43 ± 0.12	≤ 25.9	≤ 25.9	NA	−0.59
J0224.2–0003	02 24 12.85	2.9	−00 03 12.2	2.4	4.45	S	0.59 ± 0.15	≤ 32.3	≤ 24.8	86 ± 42	−0.92
J0224.2–0528*	02 24 14.74	2.2	−05 28 40.6	2.3	0.98	M	1.61 ± 0.23	≤ 42.6			−0.76
	02 24 13.15	2.9	−05 28 05.2	2.9	0.97	C	1.04 ± 0.19	≤ 49.2	≤ 43.9	NA	−0.76
	02 24 14.74	2.2	−05 28 40.6	2.3	0.98	C	0.57 ± 0.11	≤ 28.8	≤ 20.6	11 ± 27	−0.76
J0224.5–0219	02 24 30.53	2.7	−02 19 32.9	2.5	2.17	S	0.37 ± 0.10	≤ 25.9	≤ 25.9	NA	−0.65
J0224.7–0732	02 24 43.05	3.6	−07 32 38.3	2.7	3.04	S	0.46 ± 0.14	≤ 42.3	≤ 26.5	76 ± 23	−0.81
J0224.7–0302	02 24 45.80	2.3	−03 02 04.9	4.4	1.47	S	1.64 ± 0.22	77.2 ± 12.9	≤ 16.1	16 ± 2	−0.81
J0225.0–0536*	02 25 05.19	1.9	−05 36 47.7	1.7	1.12	S	1.62 ± 0.15	≤ 26.9	≤ 16.8	37 ± 8	−0.65
J0225.1+0017	02 25 08.06	2.0	+00 17 08.2	1.9	4.79	S	1.59 ± 0.19	≤ 30.7	≤ 15.4	22 ± 8	−0.59
J0225.1–0035	02 25 08.09	1.8	−00 35 31.1	1.5	3.91	S	6.45 ± 0.35	≤ 17.6	≤ 6.9	46 ± 3	−0.58
J0225.1–0739	02 25 09.52	2.3	−07 39 14.9	2.1	3.16	M	1.87 ± 0.25	≤ 39.6			−0.60
	02 25 08.35	2.8	−07 38 39.3	2.5	3.15	C	1.19 ± 0.20	≤ 52.3	≤ 31.4	51 ± 10	−0.60
	02 25 09.52	2.3	−07 39 14.9	2.1	3.16	C	0.68 ± 0.13	≤ 24.4	≤ 22.2	NA	−0.60
J0225.2–0930	02 25 15.37	4.8	−09 30 58.9	4.6	5.02	S	0.97 ± 0.27	≤ 81.4	≤ 29.4	46 ± 7	−0.76
J0225.5–0210	02 25 34.29	2.5	−02 10 16.5	2.4	2.34	S	0.54 ± 0.12	≤ 31.0	≤ 22.4	37 ± 30	−0.07
J0226.3–0425*	02 26 19.58	2.3	−04 25 37.1	2.7	0.42	S	0.54 ± 0.12	≤ 36.9	≤ 22.5	175 ± 17	−0.89
J0226.4–0846	02 26 24.97	2.7	−08 46 30.0	2.0	4.30	S	1.82 ± 0.25	34.9 ± 10.9	≤ 27.4	70 ± 6	−0.60
J0226.5–0806	02 26 34.26	2.2	−08 06 16.5	2.0	3.63	S	1.17 ± 0.17	≤ 33.9	≤ 23.9	51 ± 16	−0.67
J0226.5–0715	02 26 35.52	2.6	−07 15 04.7	2.6	2.79	S	0.57 ± 0.13	≤ 36.2	≤ 22.6	38 ± 19	−0.86
J0226.6–0121	02 26 39.55	2.6	−01 21 17.3	2.4	3.18	S	0.68 ± 0.14	≤ 34.8	≤ 24.6	44 ± 24	−1.01
J0226.7–0712	02 26 45.03	2.6	−07 12 11.8	2.9	2.75	S	1.02 ± 0.19	≤ 51.5	≤ 30.3	27 ± 10	−0.89
J0226.9–0555	02 26 59.23	1.8	−05 55 45.0	1.6	1.54	S	2.47 ± 0.17	≤ 18.3	≤ 12.2	39 ± 10	−0.77
J0227.2–0053	02 27 12.59	2.2	−00 53 43.1	2.0	3.66	S	0.66 ± 0.13	≤ 20.8	≤ 20.6	NA	−0.98
J0227.6–0908	02 27 40.73	9.1	−09 08 51.8	3.5	4.71	S	1.72 ± 0.38	94.2 ± 24.7	≤ 34.5	74 ± 3	−0.94
J0227.7–0250	02 27 44.13	2.5	−02 50 47.2	2.3	1.82	S	0.42 ± 0.10	≤ 23.9	≤ 23.9	NA	−0.76
J0228.0–0644	02 28 02.23	2.8	−06 44 38.2	2.5	2.40	S	0.40 ± 0.11	≤ 28.7	≤ 25.7	NA	−0.60
J0228.1+0031	02 28 06.05	2.1	+00 31 18.9	2.0	5.09	S	1.19 ± 0.19	≤ 27.9	≤ 18.2	42 ± 18	−0.52
J0228.1–0231	02 28 07.62	1.8	−02 31 06.8	1.6	2.16	S	1.72 ± 0.14	≤ 18.9	≤ 13.8	4 ± 17	−0.90
J0228.1–0115	02 28 07.79	1.8	−01 15 42.9	1.5	3.35	S	4.13 ± 0.25	≤ 21.9	≤ 15.8	27 ± 7	−0.75
J0228.1–0046	02 28 10.86	2.6	−00 46 00.2	2.4	3.83	S	0.50 ± 0.13	≤ 24.5	≤ 24.5	NA	−0.73

Table 3—Continued

Source	α (J2000) (h m s)	σ_α ($''$)	δ (J2000) ($^\circ$ ' $''$)	σ_δ ($''$)	Dist. ($^\circ$)	T.	S_{int} Jy	major ($''$)	Size minor ($''$)	PA ($^\circ$)	α
J0228.4–0223	02 28 29.24	2.4	–02 23 18.2	2.2	2.32	S	0.48 ± 0.11	≤ 22.6	≤ 22.6	NA	–0.75
J0228.6–0602	02 28 40.45	2.1	–06 02 42.6	1.9	1.84	S	1.10 ± 0.14	≤ 32.7	≤ 19.3	38 ± 10	–0.80
J0228.7–0617	02 28 47.98	1.9	–06 17 52.6	1.7	2.07	S	1.50 ± 0.14	≤ 25.3	≤ 13.0	143 ± 8	–0.93
J0228.8–0337	02 28 53.24	1.8	–03 37 36.8	1.5	1.37	S	5.76 ± 0.31	≤ 14.9	≤ 6.2	174 ± 4	–0.62
J0229.0–0541	02 29 05.62	2.1	–05 41 09.4	1.8	1.62	S	1.39 ± 0.15	≤ 32.0	≤ 24.1	63 ± 15	–0.64
J0229.1–0656	02 29 09.92	2.1	–06 56 03.1	1.9	2.68	M	1.14 ± 0.18	94.2			–0.94
	02 29 04.36	3.3	–06 55 18.0	2.9	2.66	C	0.39 ± 0.12	≤ 37.9	≤ 28.7	62 ± 43	–0.94
	02 29 09.92	2.1	–06 56 03.1	1.9	2.68	C	0.76 ± 0.12	≤ 23.5	≤ 18.5	151 ± 36	–0.94
J0229.2–0442*	02 29 15.92	1.8	–04 42 13.1	1.5	1.16	S	3.14 ± 0.19	≤ 17.9	≤ 10.7	56 ± 6	–0.74
J0229.6+0025	02 29 37.38	2.3	+00 25 05.1	2.0	5.07	M	2.04 ± 0.28	38.2			–0.77
	02 29 37.38	2.3	+00 25 05.1	2.0	5.07	C	1.31 ± 0.21	≤ 33.5	≤ 22.5	50 ± 16	–0.77
	02 29 39.36	2.5	+00 25 29.2	2.2	5.08	C	0.73 ± 0.17	≤ 26.4	≤ 23.0	NA	–0.77
J0229.7–0705	02 29 42.95	1.9	–07 05 37.1	1.7	2.88	S	2.29 ± 0.20	≤ 33.4	≤ 22.5	120 ± 7	–0.91
J0229.7–0206	02 29 47.33	2.7	–02 06 47.2	2.5	2.71	S	0.57 ± 0.13	≤ 31.2	≤ 30.2	NA	–0.79
J0230.0–0331	02 30 01.53	3.5	–03 31 53.5	2.6	1.65	S	0.40 ± 0.12	≤ 41.3	≤ 26.4	83 ± 24	–0.91
J0230.1–0642	02 30 10.94	2.2	–06 42 27.7	2.2	2.60	S	0.85 ± 0.14	≤ 31.6	≤ 23.6	14 ± 23	–1.17
J0230.2–0750	02 30 17.55	2.4	–07 50 38.1	2.2	3.62	S	0.57 ± 0.12	≤ 22.3	≤ 22.3	NA	–0.53
J0230.3–0255	02 30 21.99	1.8	–02 55 03.8	1.6	2.13	S	2.06 ± 0.15	≤ 15.6	≤ 15.0	NA	–1.08
J0230.3–0412	02 30 23.46	2.0	–04 12 29.5	1.9	1.46	S	0.74 ± 0.11	≤ 21.8	≤ 17.7	172 ± 42	–0.42
J0230.4–0830	02 30 25.58	2.1	–08 30 43.0	1.9	4.26	S	1.87 ± 0.22	≤ 37.4	≤ 23.8	36 ± 9	–0.71
J0230.5–0638	02 30 34.98	3.2	–06 38 40.9	3.7	2.60	S	0.44 ± 0.14	≤ 49.4	≤ 27.0	148 ± 17	–0.84
J0230.6–0409	02 30 36.80	2.5	–04 09 37.5	1.9	1.52	S	0.73 ± 0.12	≤ 33.9	≤ 19.2	82 ± 12	–0.71
J0230.6–0328	02 30 40.77	2.7	–03 28 39.2	2.1	1.81	S	0.75 ± 0.14	≤ 38.8	≤ 25.2	92 ± 16	–0.85
J0230.7–0701	02 30 43.38	2.1	–07 01 21.6	2.1	2.94	S	0.81 ± 0.13	≤ 29.0	≤ 19.4	172 ± 19	–0.84
J0230.7–0840	02 30 43.74	4.0	–08 40 37.4	3.7	4.44	S	0.77 ± 0.23	≤ 55.4	≤ 39.5	51 ± 26	–0.89
J0230.9–0909	02 30 54.66	2.6	–09 09 50.7	2.6	4.92	S	1.30 ± 0.23	≤ 50.9	≤ 21.5	40 ± 6	–0.62
J0230.9–0624	02 30 58.17	2.7	–06 24 47.3	2.3	2.47	S	0.50 ± 0.12	≤ 29.9	≤ 23.2	101 ± 42	–0.71
J0231.0–0049	02 31 01.10	3.0	–00 49 44.4	2.8	4.00	S	0.39 ± 0.13	≤ 28.6	≤ 28.5	NA	–1.01
J0231.0–0013	02 31 02.83	2.5	–00 13 59.3	2.3	4.55	S	2.26 ± 0.30	≤ 45.0	≤ 43.4	NA	–0.97
J0231.4–0314	02 31 26.70	4.0	–03 14 58.2	2.9	2.10	S	0.38 ± 0.13	≤ 45.8	≤ 28.2	77 ± 23	–0.86
J0231.4–0421	02 31 26.71	1.8	–04 21 34.3	1.6	1.70	S	1.83 ± 0.15	≤ 21.6	≤ 14.0	40 ± 10	–0.60
J0231.5–0228	02 31 31.62	2.5	–02 28 03.5	2.4	2.66	S	0.43 ± 0.11	≤ 24.4	≤ 24.4	NA	–0.49
J0231.6–0452	02 31 40.58	2.2	–04 52 58.8	1.8	1.79	M	3.05 ± 0.28	50.3			–0.82
	02 31 37.35	2.5	–04 53 13.1	2.2	1.78	C	1.13 ± 0.17	≤ 45.1	≤ 28.4	55 ± 10	–0.82
	02 31 40.58	2.2	–04 52 58.8	1.8	1.79	C	1.93 ± 0.20	28.6 ± 9.7	≤ 33.3	85 ± 13	–0.82
J0231.8–0226	02 31 51.96	2.8	–02 26 44.2	2.2	2.73	S	0.63 ± 0.14	≤ 37.4	≤ 21.7	65 ± 15	–0.79
J0232.1–0627	02 32 08.78	2.7	–06 27 21.4	2.5	2.70	S	0.39 ± 0.11	≤ 25.8	≤ 25.8	NA	–0.47
J0232.2–0441	02 32 14.11	1.9	–04 41 50.6	1.7	1.90	S	1.32 ± 0.13	≤ 24.2	≤ 14.4	39 ± 11	–0.76
J0232.2–0749	02 32 15.68	2.9	–07 49 48.4	2.2	3.83	S	0.80 ± 0.17	≤ 42.6	≤ 21.2	112 ± 10	–0.71
J0232.5–0418	02 32 32.88	4.5	–04 18 27.4	3.4	1.97	S	0.50 ± 0.15	≤ 60.9	≤ 29.9	121 ± 13	–0.59
J0232.7–0632	02 32 44.61	3.1	–06 32 08.3	2.9	2.86	S	0.36 ± 0.12	≤ 33.2	≤ 28.2	NA	–0.56
J0232.7–0234	02 32 45.68	2.5	–02 34 25.1	3.7	2.79	M	4.07 ± 0.41	93.7			–0.87
	02 32 42.25	3.3	–02 33 06.8	2.2	2.80	C	1.66 ± 0.25	44.0 ± 11.3	≤ 38.7	91 ± 8	–0.87
	02 32 45.68	2.5	–02 34 25.1	3.7	2.79	C	2.41 ± 0.30	70.8 ± 11.2	≤ 36.3	158 ± 3	–0.87
J0232.8–0425	02 32 49.59	3.5	–04 25 31.9	2.4	2.04	S	0.46 ± 0.13	≤ 42.3	≤ 25.0	86 ± 18	–0.57
J0232.8+0017	02 32 50.31	4.7	+00 17 19.7	2.7	5.21	S	0.75 ± 0.23	≤ 58.7	≤ 26.5	81 ± 11	–0.53
J0232.8–0645	02 32 53.96	1.8	–06 45 51.4	1.5	3.05	S	8.79 ± 0.46	≤ 18.8	≤ 14.1	174 ± 4	–0.62
J0233.2–0012	02 33 13.49	3.2	–00 12 14.5	2.1	4.80	S	1.77 ± 0.28	41.0 ± 12.0	≤ 27.1	74 ± 5	–0.93
J0233.3–0320	02 33 18.52	2.0	–03 20 54.7	1.5	2.44	S	6.06 ± 0.37	64.4 ± 4.9	≤ 18.1	84 ± 1	–0.74
J0233.3–1000	02 33 21.53	1.9	–10 00 23.4	1.7	5.91	S	5.91 ± 0.45	31.3 ± 7.3	≤ 29.7	27 ± 6	–0.84
J0233.4–0455	02 33 24.18	3.3	–04 55 00.7	1.9	2.22	S	0.94 ± 0.16	≤ 56.1	≤ 18.9	87 ± 5	–0.51
J0233.4–0713	02 33 28.79	2.4	–07 13 28.5	2.6	3.50	S	0.79 ± 0.16	≤ 37.4	≤ 26.3	1 ± 21	–0.81
J0233.5–0203	02 33 30.46	1.8	–02 03 22.5	1.6	3.29	S	1.88 ± 0.15	≤ 17.5	≤ 11.8	31 ± 15	–0.61
J0233.6–0912	02 33 40.53	3.2	–09 12 33.8	2.9	5.21	S	0.80 ± 0.21	≤ 46.2	≤ 25.8	49 ± 15	–0.82
J0233.7–0232	02 33 43.86	2.1	–02 32 11.7	1.7	3.00	S	1.83 ± 0.18	26.4 ± 9.8	≤ 13.2	66 ± 3	–0.88
J0233.9–0507	02 33 56.91	2.2	–05 07 53.3	3.0	2.40	M	2.53 ± 0.30	62.2			–1.21
	02 33 56.91	2.2	–05 07 53.3	3.0	2.40	C	1.66 ± 0.23	45.3 ± 10.8	≤ 33.3	177 ± 6	–1.21
	02 33 57.94	2.6	–05 08 53.6	3.3	2.40	C	0.88 ± 0.18	≤ 52.8	≤ 31.2	168 ± 12	–1.21
J0234.1–0603	02 34 11.94	2.4	–06 03 58.7	2.3	2.84	S	1.12 ± 0.18	≤ 40.1	≤ 30.3	30 ± 19	–0.82
J0234.2–0935	02 34 15.91	4.4	–09 35 13.1	3.8	5.62	S	1.12 ± 0.33	≤ 58.1	≤ 48.6	NA	–0.20
J0234.3–0523	02 34 21.49	2.3	–05 23 35.2	2.0	2.57	S	0.68 ± 0.12	≤ 27.2	≤ 19.8	107 ± 28	–0.91
J0234.3–0139	02 34 21.85	2.6	–01 39 00.5	2.4	3.74	S	0.48 ± 0.12	≤ 24.8	≤ 24.6	NA	–0.64
J0234.3–0645	02 34 22.75	2.1	–06 45 11.8	1.9	3.30	M	2.10 ± 0.23	40.4			–0.85
	02 34 22.75	2.1	–06 45 11.8	1.9	3.30	C	0.98 ± 0.14	≤ 28.1	≤ 20.0	139 ± 20	–0.85
	02 34 23.96	2.2	–06 45 48.0	2.2	3.31	C	1.12 ± 0.17	≤ 38.0	≤ 22.8	35 ± 11	–0.85
J0234.4–0013	02 34 27.09	2.4	–00 13 38.9	2.1	4.92	S	0.87 ± 0.17	≤ 27.7	≤ 20.7	64 ± 32	–0.56

Table 3—Continued

Source	α (J2000) (h m s)	σ_α ($''$)	δ (J2000) ($^\circ$ ' $''$)	σ_δ ($''$)	Dist. ($^\circ$)	T.	S_{int} Jy	major ($''$)	Size minor ($''$)	PA ($^\circ$)	α
J0234.7–0050	02 34 45.77	2.4	–00 50 23.4	2.1	4.44	S	0.88 ± 0.17	≤ 31.7	≤ 20.1	49 ± 18	–0.57
J0234.9–0736	02 34 58.35	2.1	–07 36 18.6	1.9	4.03	S	0.83 ± 0.14	≤ 22.1	≤ 19.2	NA	–0.73
J0235.1–0402	02 35 07.03	1.8	–04 02 04.6	1.5	2.65	M	10.46 ± 0.56	55.7			–0.66
	02 35 07.03	1.8	–04 02 04.6	1.5	2.65	C	9.65 ± 0.50	≤ 20.4	≤ 12.5	79 ± 2	–0.66
	02 35 10.36	4.1	–04 01 39.8	2.1	2.66	C	0.81 ± 0.17	≤ 62.6	≤ 21.2	96 ± 6	–0.66
J0235.5–0219	02 35 32.59	1.8	–02 19 31.9	1.5	3.48	S	4.71 ± 0.28	≤ 21.6	≤ 10.9	52 ± 4	–0.54
J0235.6–0759	02 35 41.76	3.4	–07 59 58.6	3.7	4.45	S	0.95 ± 0.24	≤ 53.0	≤ 42.2	26 ± 34	–0.68
J0235.9–0803	02 35 54.60	2.7	–08 03 47.4	3.4	4.53	S	1.16 ± 0.24	≤ 53.5	≤ 35.3	168 ± 15	–0.75
J0236.1–0250	02 36 06.45	2.6	–02 50 11.4	2.0	3.30	S	0.82 ± 0.15	≤ 37.7	≤ 19.7	75 ± 11	–0.89
J0236.3–0437	02 36 21.41	2.7	–04 37 37.9	2.4	2.92	S	0.57 ± 0.13	≤ 35.4	≤ 22.8	48 ± 21	–0.78
J0237.1–0348	02 37 10.31	1.9	–03 48 26.0	1.6	3.19	S	1.85 ± 0.17	≤ 27.6	≤ 12.5	56 ± 6	–0.76
J0237.9–0145	02 37 57.23	1.8	–01 45 11.4	1.6	4.31	S	3.28 ± 0.23	≤ 24.4	≤ 13.3	52 ± 5	–0.73
J0238.2–0628	02 38 14.11	2.3	–06 28 52.6	1.9	3.92	S	0.99 ± 0.16	≤ 31.1	≤ 18.2	71 ± 13	–0.55
J0238.3–0330	02 38 18.82	1.8	–03 30 17.3	1.6	3.55	S	2.58 ± 0.20	≤ 24.1	≤ 16.0	66 ± 8	–0.68
J0238.3–0616	02 38 23.54	2.3	–06 16 16.1	1.8	3.85	M	2.05 ± 0.24	67.5			–0.80
	02 38 23.54	2.3	–06 16 16.1	1.8	3.85	C	1.06 ± 0.16	≤ 31.7	≤ 17.6	77 ± 11	–0.80
	02 38 28.07	2.4	–06 16 15.8	2.0	3.87	C	0.99 ± 0.17	≤ 32.5	≤ 23.1	84 ± 20	–0.80
J0238.5–0432	02 38 35.12	2.3	–04 32 41.2	2.1	3.47	S	0.65 ± 0.13	≤ 23.7	≤ 20.8	NA	–0.62
J0238.9–0255	02 38 57.01	3.5	–02 55 11.0	2.5	3.90	S	0.86 ± 0.19	≤ 51.4	≤ 28.4	69 ± 12	–0.63
J0239.2–0118	02 39 13.70	1.9	–01 18 16.3	1.7	4.84	S	2.27 ± 0.21	≤ 29.9	≤ 13.6	48 ± 6	–0.76
J0239.7–0117	02 39 42.60	2.4	–01 17 22.0	2.2	4.94	S	1.16 ± 0.20	≤ 38.9	≤ 19.0	45 ± 9	–0.83
J0240.6–0723	02 40 36.79	2.7	–07 23 16.1	2.7	4.91	S	0.85 ± 0.20	≤ 38.6	≤ 26.3	146 ± 22	–0.49
J0240.6–0638	02 40 39.25	4.2	–06 38 26.4	3.4	4.52	S	1.10 ± 0.27	≤ 58.8	≤ 47.4	89 ± 34	–0.68
J0240.6–0446	02 40 40.97	2.5	–04 46 18.9	2.0	4.00	S	1.03 ± 0.17	≤ 38.5	≤ 19.7	69 ± 9	–0.62
J0241.6–0418	02 41 36.23	2.5	–04 18 21.8	1.9	4.23	S	1.21 ± 0.19	≤ 38.9	≤ 20.2	74 ± 9	–0.47
J0241.6–0647	02 41 38.00	1.8	–06 47 30.4	1.6	4.80	S	4.57 ± 0.31	≤ 25.4	≤ 25.4	NA	–0.61
J0241.6–0348	02 41 38.42	3.9	–03 48 45.3	3.0	4.29	S	0.67 ± 0.19	≤ 50.8	≤ 31.8	65 ± 20	–0.81
J0242.1–0128	02 42 07.95	4.3	–01 28 35.2	2.4	5.31	S	1.06 ± 0.25	≤ 63.0	≤ 22.8	75 ± 7	–0.60
J0242.3–0240	02 42 18.77	3.0	–02 40 38.4	2.8	4.76	S	0.45 ± 0.15	≤ 28.8	≤ 28.5	NA	–0.50
J0242.3–0409	02 42 23.02	3.2	–04 09 02.0	2.6	4.43	S	0.64 ± 0.17	≤ 41.3	≤ 24.5	118 ± 18	–0.68
J0242.7–0311	02 42 42.94	4.2	–03 11 44.9	2.3	4.69	S	1.40 ± 0.27	44.7 ± 14.6	≤ 27.9	100 ± 6	–0.50
J0242.7–0157	02 42 47.59	2.3	–01 57 47.7	2.0	5.19	S	1.40 ± 0.21	≤ 36.7	≤ 17.6	56 ± 8	–0.64
J0243.2–0356	02 43 17.29	3.3	–03 56 51.6	2.8	4.67	S	0.46 ± 0.15	≤ 33.9	≤ 28.4	NA	–0.35
J0243.5–0232	02 43 31.41	2.6	–02 32 55.3	2.3	5.09	S	1.20 ± 0.23	≤ 36.1	≤ 31.0	68 ± 45	–0.40
J0243.8–0305	02 43 53.30	3.0	–03 05 06.0	2.9	5.00	S	0.83 ± 0.21	≤ 37.9	≤ 36.5	NA	–0.52
J0244.3–0427	02 44 20.44	3.4	–04 27 47.7	2.2	4.90	S	0.94 ± 0.21	≤ 49.2	≤ 21.9	81 ± 9	–0.49
J0244.3–0653	02 44 23.00	2.4	–06 53 27.8	1.9	5.46	S	1.48 ± 0.23	≤ 34.2	≤ 22.3	83 ± 14	–0.73
J0244.4–0527	02 44 26.47	2.3	–05 27 17.2	1.9	5.02	S	1.85 ± 0.24	≤ 38.5	≤ 24.6	81 ± 10	–0.69
J0244.9–0447	02 44 57.67	2.9	–04 47 48.5	2.7	5.07	S	0.50 ± 0.16	≤ 28.9	≤ 27.6	NA	–0.87
J0245.1–0133	02 45 09.72	2.6	–01 33 49.5	2.1	5.90	S	1.22 ± 0.23	≤ 35.8	≤ 20.3	72 ± 14	–0.81
J0246.3–0449	02 46 22.65	2.4	–04 49 34.2	2.8	5.42	S	2.36 ± 0.34	41.0 ± 11.2	≤ 33.4	25 ± 7	–0.72
J0247.1–0354	02 47 09.69	3.2	–03 54 49.7	3.0	5.64	S	0.56 ± 0.19	≤ 33.8	≤ 28.6	NA	–0.67
J0247.2–0554	02 47 16.29	4.0	–05 54 40.5	2.7	5.80	S	1.24 ± 0.30	≤ 57.4	≤ 32.4	101 ± 13	–0.47

Note. — An asterisk (*) after the sourcename indicates this source was also detected at 325 MHz.

Note. — Positions of multiple sources are given as the position of the peak component.

Note. — Description of columns:

1. Source Name
2. Right Ascension (J2000)
3. Right Ascension uncertainty in arcseconds
4. Declination (J2000)
5. Declination uncertainty in arcseconds
6. Distance from pointing center in degrees
7. Source type: Single (S), Multiple (M) or Component (C) of multiple source
8. Integrated Flux in Jy
9. Size of Major Axis in arcseconds, or the 2σ upper limit if the source is unresolved
10. Size of Minor Axis in arcseconds, or the 2σ upper limit if the source is unresolved
11. PA of Major axis in degrees.
12. Spectral index with respect to NVSS flux (1.4 GHz).

Table 4. Objects with known redshifts

Object	RA (J2000)	DEC (J2000)	Object Type	Redshift	Reference
J0210.8–0633	2 10 53.06	–6 33 38.3	Galaxy	0.04340	Tovmassian et al. (1999)
J0213.7–0256	2 13 46.80	–2 56 39.8	Galaxy	0.35680 ± 0.00020	Owen, Ledlow, & Keel (1995)
J0215.1–0702	2 15 07.65	–7 02 06.4	QSO	2.22000	Becker et al. (2001)
J0215.6–0222	2 15 41.98	–2 22 52.0	QSO	1.17800	Drinkwater et al. (1997)
J0217.4–0052	2 17 28.57	–0 52 27.8	QSO	2.45476 ± 0.00165	Sloan Digital Sky Survey (2001)
J0219.1+0120	2 19 07.25	+1 20 58.3	QSO	1.62300	The NED Team (1992)
J0220.5+0027	2 20 33.43	+0 27 57.7	Galaxy	0.27226 ± 0.00016	Sloan Digital Sky Survey (2001)
J0220.9–0156	2 20 54.26	–1 56 52.5	Galaxy	0.17500	Hewitt & Burbidge (1991)
J0225.1+0017	2 25 08.06	+0 17 08.2	QSO	0.52300	Dunlop et al. (1989)
J0225.1–0035	2 25 08.09	–0 35 31.1	QSO	0.68700	Dunlop et al. (1989)
J0228.1–0115	2 28 07.78	–1 15 42.9	QSO	2.03700	Dunlop et al. (1989)
J0228.8–0337	2 28 53.24	–3 37 36.8	QSO	2.05500 ± 0.00100	Osmer, Porter, & Green (1994)
J0231.0–0049	2 31 01.10	–0 49 44.4	Galaxy	0.33952 ± 0.00012	Sloan Digital Sky Survey (2001)
J0233.2–0012	2 33 13.49	–0 12 14.5	QSO	0.81000	Becker et al. (2001)
J0233.5–0203	2 33 30.46	–2 03 22.5	Galaxy	0.79400	Dunlop et al. (1989)
J0234.3–0139	2 34 21.85	–1 39 00.5	Galaxy	0.64500 ± 0.00200	Stanford et al. (2000)
J0235.1–0402	2 35 07.03	–4 02 04.6	QSO	1.45000 ± 0.00300	Stocke et al. (1991)
J0235.5–0219	2 35 32.59	–2 19 31.9	QSO	1.32100	Dunlop et al. (1989)
J0237.9–0145	2 37 57.23	–1 45 11.4	Galaxy	0.84000	Dunlop et al. (1989)
J0239.2–0118	2 39 13.70	–1 18 16.3	QSO	1.79400	Dunlop et al. (1989)
J0242.6–0000	2 42 40.66	–0 00 47.0	Galaxy	0.00379 ± 0.00001	Huchra, Vogeley, & Geller (1999)
J0242.7–0157	2 42 47.59	–1 57 47.7	QSO	0.61700	Dunlop et al. (1989)